

# STUDY OF THE DETONATION PHASE IN THE GRAVITATIONALLY CONFINED DETONATION MODEL OF TYPE Ia SUPERNOVAE

Casey A. Meakin<sup>1,2,3,5</sup>, Ivo Seitenzahl<sup>3,4</sup>, Dean Townsley<sup>1,2,3</sup>, George C. Jordan IV<sup>1,2</sup>, James Truran<sup>1,2,3</sup>,  
Don Lamb<sup>1,2,4</sup>

casey.meakin@gmail.com

## ABSTRACT

We study the gravitationally confined detonation (GCD) model of Type Ia supernovae through the detonation phase and into homologous expansion. In the GCD model, a detonation is triggered by the surface flow due to single point, off-center flame ignition in carbon-oxygen white dwarfs. The simulations are unique in terms of the degree to which non-idealized physics is used to treat the reactive flow, including weak reaction rates and a time dependent treatment of material in nuclear statistical equilibrium (NSE). Careful attention is paid to accurately calculating the final composition of material which is burned to NSE and frozen out in the rapid expansion following the passage of a detonation wave over the high density core of the white dwarf; and an efficient method for nucleosynthesis post-processing is developed which obviates the need for costly network calculations along tracer particle thermodynamic trajectories. Observational diagnostics are presented for the explosion models, including abundance stratifications and integrated yields. We find that for all of the ignition conditions studied here, a self regulating process comprised of neutronization and stellar expansion results in final  $^{56}\text{Ni}$  masses of  $\sim 1.1M_{\odot}$ . But, more energetic models result in larger total NSE and stable Fe peak yields. The total yield of intermediate mass elements is  $\sim 0.1M_{\odot}$  and the explosion energies are all around  $1.5 \times 10^{51}$  ergs. The explosion models are briefly compared to the inferred properties of recent Type Ia supernova observations. The potential for surface detonation models to produce lower luminosity (lower  $^{56}\text{Ni}$  mass) supernovae is discussed.

*Subject headings:* stars: evolution - stars: nucleosynthesis - supernovae - hydrodynamics

## 1. INTRODUCTION

The currently favored model for Type Ia supernovae (SNe Ia) is the thermonuclear incineration of a white dwarf (WD) which has accreted mass to near the Chandrasekhar limit from a binary companion (e.g., Branch et al. 1995; Hillebrandt & Niemeyer 2000). The enormous luminosity and homogeneity in the properties of the light curves of SNe Ia make them exceptionally good standard candles and as such

---

<sup>1</sup>Center for Astrophysical Thermonuclear Flashes, University of Chicago, Chicago, IL

<sup>2</sup>Department of Astronomy and Astrophysics, University of Chicago, Chicago, IL

<sup>3</sup>Joint Institute for Nuclear Astrophysics, University of Chicago, Chicago, IL

<sup>4</sup>Enrico Fermi Institute, University of Chicago, Chicago, IL

<sup>5</sup>Steward Observatory, University of Arizona, Tucson, AZ

have shown that the expansion rate of the universe is accelerating and provided intriguing evidence for a cosmological constant (Riess et al. 1998).

Despite the success in using SNe Ia as cosmological probes and identifying a plausible astrophysical progenitor site for the explosions, a detailed understanding of the explosion mechanisms itself remains elusive. Several uncertainties stand in the way of a definitive solution to the SNe Ia problem. On the one hand, the conditions under which the thermonuclear runaway commences remains poorly understood so that the initial number and distribution of flamelets that seed the runaway is still a free parameter. On the other hand, although significant progress has been made in simulating flame fronts in multi-dimensional stellar models (Gamezo et al. 2005; Schmidt et al. 2006b; Röpke et al. 2007a; Townsley et al. 2007; Jordan et al. 2008), the challenge associated with modeling an unresolved turbulent deflagration (e.g. Schmidt et al. 2006a) with limited computational resources injects an additional degree of uncertainty into the outcome of a model for any given choice of initial conditions.

In this paper we describe progress on our ongoing effort to improve the simulation of SNe Ia in multi-dimensions, including methods to perform detailed nucleosynthesis post-processing in a computationally efficient manner. We extend the study of the GCD model for a single ignition point slightly offset a range of distances from the center of the star, as described in Townsley et al. (2007), through the detonation phase and into homologous expansion. In §2 we describe the treatment of the reactive-hydrodynamics problem used in our simulation code. In §3 we review the relevant properties of the deflagration phase for single point flame ignition. In §4 we examine in some detail the initiation of the detonation, the properties of the detonation wave which disrupts the star, and the resultant remnant morphology. In §5 we discuss in detail the nucleosynthetic yields for the explosions studied and describe the methodology used to efficiently calculate iron peak yields from the simulation data. We conclude with a summary of the salient features of the explosion models in light of observed Type Ia supernovae.

## 2. NUMERICAL METHODS: HYDRODYNAMICS AND NUCLEAR BURNING

In this section we review the computational tools used to model the hydrodynamic and nuclear evolution of the stellar plasma, including the treatment of subsonic (deflagration) and supersonic (detonation) burning fronts. The basic code framework is FLASH (Fryxell et al. 2000), a modular, block-structured adaptive mesh refinement (AMR), Eulerian, reactive-hydrodynamics code. We use a directionally split PPM solver (Colella & Woodward 1984) generalized to treat non-ideal gasses (Colella & Glaz 1985) to handle the hydrodynamic evolution.

The energetics scheme used to treat flames and detonation waves in our simulations uses 3 progress variables to track carbon burning, NSQE relaxation, and NSE relaxation. The rates connecting these burning stages are calibrated using a large (200 nuclide) nuclear reaction network for the conditions relevant to the Type Ia problem. Additionally, energy losses (through neutrino emission) and changes in the electron mole fraction  $Y_e$  due to weak interactions taking place in material which has burned to NSE are incorporated. Details can be found in Calder et al. (2007); Townsley et al. (2007); Seitenzahl et al. (2008a).

Both detonation waves and flames are impossible to resolve in full star simulations because they are characterized by length scales that are more than ten orders of magnitude smaller than the radius of the white dwarf to be modeled,  $R_{\text{wd}} \sim 10^8$  cm. Therefore, these reaction fronts must be treated in a special manner. Subsonic burning fronts (deflagrations) are advanced using an advection-diffusion-reaction (ADR) equation. In short, a thickened flame front ( $\sim 4$  grid zones wide) is advanced at a speed  $v_f = \max(v_l, v_t)$ ,

where  $v_l$  is the laminar flame speed calculated by Timmes & Woosley (1992) and  $v_t$  is a Rayleigh-Taylor driven turbulent flame speed. Details concerning the implementation, calibration and noise properties of the flame treatment can be found in Townsley et al. (2007) and Asida et al. (2008, in preparation) and references therein.

Detonations are handled naturally by the reactive hydrodynamics solver in FLASH without the need for a front tracker. This approach is possible because unresolved Chapman-Jouguet (CJ) detonations retain the correct jump conditions and propagation speeds. Numerical stability is maintained by preventing nuclear burning within the shock. This is necessary because shocks are artificially spread out over a few zones by the PPM hydrodynamics solver, which can lead to unphysical burning within shocks that can destabilize the burning front (Fryxell, Mueller & Arnett 1989). The energetics in the detonation differ from that in the deflagration front only in how carbon burning proceeds, as represented by the first progress variable  $\phi_1$  and an explicit carbon burning rate is used (Caughlan & Fowler 1988). The additional burning stages (NSQE and NSE relaxation) are tracked by  $\phi_2$  and  $\phi_3$  and are evolved in the same manner as in the post flame ash (Calder et al. 2007; Townsley et al. 2007). At densities above  $\sim 10^7 \text{ g cm}^{-3}$  detonations propagating through a mixture that is equal parts  $^{12}\text{C}$  and  $^{16}\text{O}$  have Mach numbers that are larger than the CJ value, but by only a few percent (Gamezo et al. 1999; Sharpe 2001). Cellular structure smaller than the grid scale will be suppressed in our simulations but is free to form on resolved scales. The impact of cellular structure on the global evolution of the model is still uncertain. However, since cellular structure alters the detonation wave speed by only a few percent for the conditions being modeled (Timmes et al. 2000b) the effect is likely to be small. Additional details related to the treatment of detonation waves are discussed in §4.

Self gravity is calculated using a multi-pole solver with a maximum spherical harmonic index  $l_{max}=10$ . The Helmholtz equation of state of Timmes & Swesty (2000a) is used to describe the thermodynamic properties of the stellar plasma including contributions from blackbody radiation, ions, and electrons of an arbitrary degree of degeneracy.

Passive tracer particles are included in our simulations which record the time history of the flow properties along Lagrangian trajectories. These records can be used to calculate detailed nucleosynthetic yields as well as to provide additional diagnostic for complex flows. We use  $10^5$  tracer particles for 2D models and  $10^6$  for 3D models. The particles used in this study are initialized at the beginning of each simulation with a mass weighted distribution. In §5.1 we present a novel method to calculate post-explosion yields which does not require the prohibitively expensive post-processing of a large number of tracer particle with a nuclear reaction network, but rather uses information readily extracted from the tracers to calibrate an efficient table look-up scheme.

### 3. FLAME IGNITION AND DEFLAGRATION

In this paper we extend the study of the GCD model for the single point flame ignition models of Townsley et al. (2007) through the detonation phase and into homologous expansion. The general simulation setup is the same, and we review it here briefly, along with a description of the basic progression of the evolution preceding detonation. After carbon burning ignites at the center of the white dwarf, a convective core is formed which expands as it heats. Our simulations begin when the nuclear burning timescale becomes shorter than the eddy turnover time, so that the first flamelet is ignited near (within a few hundred km of) the center of the white dwarf. As discussed by Townsley et al. (2007), there is still significant uncertainty in the form which the nuclear flame will take at birth (also see e.g. Woosley et al. 2004), relating to the number

and location of what are generally assumed to be relatively small ( $< 1$  km) ignition regions. For reasons related to simplicity of setup and limitations of the imposed cylindrical symmetry, we restrict our study to off-center, single point ignitions in a quiescent background star. The initial WD used in these simulations has a uniform temperature  $4 \times 10^7$  K, a mass of  $1.365 M_{\odot}$ <sup>1</sup>, a central density of  $2.2 \times 10^9$  g cm<sup>-3</sup>, and is composed of equal mass fractions of <sup>12</sup>C and <sup>16</sup>O. This progenitor is much colder than reality, but it is expected, and we have confirmed by comparison, that this does not have a significant effect on the structure of the white dwarf or the dynamics of the explosion. At the beginning of the simulation a spherical region of radius  $r_{\text{bub}}=16$  km placed on the polar axis at a range of distances between  $r_{\text{off}}=20$  and 100 km from the center of the star is converted to NSE ash in pressure equilibrium with the remainder of the star. A summary of the initial flame bubble parameters studied in this paper is given in Table 1.

The basic stages of single bubble flame evolution can be described in terms of two key length scales, the grid resolution,  $\Delta$ , which sets the limit to which we can resolve flame structure, and the critical wavelength, sometimes called the fire polishing length,  $\lambda_c \equiv 6\pi s^2/Ag$  (Khokhlov 1995), where  $s$  is the front propagation speed (flame speed) and  $A$  is the Atwood number  $A = (\rho_{\text{fuel}} - \rho_{\text{ash}})/(\rho_{\text{fuel}} + \rho_{\text{ash}})$ . Perturbations in a Rayleigh-Taylor (R-T) unstable flame front smaller than  $\lambda_c$  are “polished out” by the propagation of the flame, while those of larger scale are enhanced by R-T growth, wrinkling the flame bubble. Townsley et al. (2007) distinguished three phases of flame evolution that occur successively as the buoyant flame bubble grows in size and rises toward the stellar surface: laminar bubble growth when  $r_{\text{bub}} \lesssim \lambda_c$ , resolved R-T unstable growth, and finally R-T unstable growth on the sub-grid scale when  $\lambda_c < \Delta$ . One immediate consequence of this progression and the increase of  $g$  with radius, is that the resolution limits the largest ignition offset position  $r_{\text{off}}$  which can be used and still start in the laminar growth phase. This limit is roughly 100 km for  $\Delta = 4$  km, the resolution of all the simulations here. At this resolution the critical wavelength is less than the grid scale,  $\lambda_c < \Delta$ , outside roughly 400 km from the center of the star.

For even modest offsets, the hot ash is buoyant enough that it erupts from the surface of the star before more than a few percent of the star is burned. This creates a vigorous flow over the surface of the WD, which is still relatively compact due to the small amount of burning. The progress of this eruption and flow is shown in Figure 1 for the case with  $r_{\text{off}} = 40$  km. As mentioned previously, there is indication from comparisons of recent work (Röpke et al. 2007a; Townsley et al. 2007; Jordan et al. 2008) that the eruption pattern arising from a given offset is dependent on the choice of burning model, and therefore is currently uncertain. This has important consequences at the collision region because it sets the velocity and density structure of the incoming flows as well as the surface gravity (via the degree of stellar expansion) under which the collision occurs.

We study the cases from Townsley et al. (2007), which demonstrated collisions that created detonation conditions, along with several supplementary cases near the minimum offset distance that led to detonation conditions. This gives the range  $r_{\text{off}}=20$  to 100 km. The expansion which occurs during the deflagration and surface flow stages is very nearly homologous and has only a small degree of asymmetry, such that most of the asymmetry is created later during the detonation phase (see below). Figure 2 compares the scaled density profile for the initial model and the 25 km and 100 km offset cases at the time the detonation initiates. Density is scaled by the central value and radius is scaled by the distance from the center at which the density drops to  $1/e$  times the central value. Profiles along the equator and along the symmetry axis are both shown, demonstrating that the star remains very symmetric out to approximately 2 density scale

---

<sup>1</sup>This was erroneously given as  $1.38 M_{\odot}$  in Townsley et al. (2007), none of these parameters have changed from that work to this.

heights away from the center. This region contains approximately 90% of the stellar mass, and even the asymmetry beyond this is fairly modest, but is likely to lead to some asymmetry in the highest-velocity spectral features.

Based on the variation in expansion found in the resolution study performed by Townsley et al. (2007), and other cases generally, it appears that the conditions at the collision region and the density structure at detonation are not a single parameter family in the mass burned, or equivalently nuclear energy release, in the deflagration,  $E_{n,def}$ , prior to the collision. It does seem that  $E_{n,def}$  is the primary parameter, but other contributing factors include the time dependence of the energy release, morphology of the burning region in the flame plume, and the possibility of secondary or tertiary ignition sites. The sudden input of energy in the deflagration puts the star in an oscillation, and the timing of the detonation initiation with respect to this oscillation is important for setting the density structure at detonation, and thereby the burning products (see §5). The timing and magnitude of the nuclear energy release will change the magnitude and phase of this full-star oscillation, but further investigation, including studies of 3-dimensional deflagration morphologies, is needed to characterize these relationships.

As an aside we note the impact of neutronization due to electron captures during the deflagration. Neutronization influences the dynamics of a rising flame bubble by changing the average binding energy of the final NSE state obtained as well as the electron pressure available per gram of stellar plasma. We assessed the impact of neutronization by recalculating several models through bubble rise with weak rates suppressed, by enforcing  $\dot{Y}_e = 0$ . Flame bubbles ignited closer to the stellar center, and hence at higher densities, are more strongly affected. Models ignited at  $r_{off}=40$  km and 30 km *burned  $\sim 10\%$  and  $\sim 40\%$  more mass, respectively, with weak rates suppressed* while the model ignited at  $r_{off}=80$  km was negligibly affected by the weak reactions during bubble rise and breakout. The effect that the weak reactions have on the burned mass depends on the development of turbulence which is not well represented in the 2D simulations presented here. Therefore, while we have demonstrated that weak reactions play a non-negligible role in the present suite of models the impact that they have on more realistic 3D flows remains an open question.

#### 4. DETONATION

Single point off-center ignition results in a buoyant plume of hot ash which is brought to the surface of the star before more than a few percent of the stellar core is consumed by the flame (see  $M_{def}$  in Table 1). As the hot ash rises to the surface, the nuclear energy that is released excites a stellar pulsation which initially expands the star. Against this background pulsation, the hot ash from the burning is expelled from the stellar interior. A large fraction of this ash is confined to the star’s surface by gravity. This ash sweeps over the surface of the star together with a flow of unburned stellar material which is pushed ahead of it. In all but the most expanded model in our parameter study (i.e., those with ignition points  $r_{off} \geq 25$  km), the resulting surface flows converge at a point opposite to breakout which we refer to as the *collision region* (Fig. 1). These converging surface flows result in a bi-directional, collimated jet-like flow which both expels material away from the star’s surface and drives a flow of high temperature material into the stellar core. The inward directed component of the collimated flow reaches high enough densities and temperatures that a “surface detonation” initiates which sweeps over the core and completely disrupts the white dwarf, giving rise to a luminous supernova explosion.

In the following subsections we describe the characteristics of the bi-directional jet which forms in the colliding surface flow and initiates the detonation (§4.1), we discuss the characteristics of the ensuing

detonation phase of burning (§4.2), and we describe the final state of free expansion which results (§4.3). A detailed analysis of the nucleosynthetic yields is presented in the next section, §5.

#### 4.1. Jet Formation and Detonation Initiation

*Jet Formation and Characteristics.*— As the surface flow produced by the deflagration converges, material accumulates in a small region on the hemisphere opposite to the breakout location. The material which initially piles up, consists of unburned carbon and oxygen rich surface material which is pushed ahead of the ash as it flows around the stellar surface. As material accumulates in this region it is heated by compression until it reaches temperatures sufficient to initiate carbon burning, which further heats the compressed material and raises its pressure. Shortly after the initial collision, a conical shock forms which separates the compressed material along the axis from the inflowing surface flow. The surface flow material burns as it passes through this shock and “accretes” into the collision region. The resultant pressure in the collision region roughly balances the ram pressure of the accreting surface flow,  $p_{\text{coll}} \sim [\rho v^2]_{\text{surf}}$  (see Fig. 4). The pressure achieved in the compressed region soon exceeds the (nearly hydrostatic) background pressure sufficiently that it redirects the accreting material and drives a bidirectional jet-like flow which has components aligned along the polar axis. A closeup of the collision region thus formed is shown in Figure 3 (which corresponds to the region outlined by the dashed box in Figure 1). The velocity vectors reveal the bidirectional nature of the flow. The ash from the deflagration is just approaching the collision region at the time shown, well after the collimated jet has formed. The width of the jet increases with time as material continues to accrete into the region, but retains structure on scales  $< 50$  km, which are well resolved in our simulations which have a grid resolution of 4 km.

In Figure 4 the flow properties along the jet axis are shown just prior to the onset of detonation for two 2D models and one 3D model. The 2D models shown span the conditions studied in this paper, including the model with the most expanded core (left-panel) and the least expanded core (middle-panel) which detonate in our study. All of the collimated flows share the same overall structure with the more expanded stars having shallower density gradients in the collision region. The velocity profiles are roughly linear, decreasing from a maximum inwardly directed velocity of  $\sim (1 \text{ to } 2) \times 10^9$  cm/s to a comparable velocity directed away from the stellar surface. While the inward flow is attended by a great deal of small scale internal substructure and turbulence (Fig. 3), three distinct “fronts” are readily identifiable along the axis of the jet: a leading subsonic compression wave, followed by a fuel-ash boundary layer, and finally an internal shock. The fuel-ash boundary layer is marked in Figure 4 by the dashed vertical line. The material ahead of this line has not yet been compressed to high enough densities that carbon burning can proceed. The compression wave(s) which emanates from the head of the jet as it moves into the star can be seen as perturbations preceeding the fuel-ash boundary in all of the variables plotted in Figure 4 and can also be seen as the pressure waves extending into the star ahead of the jet in Figure 3 (left-panel). The compression wave moves into the star at the sound speed, which is  $c_s \sim 3.5 \times 10^8$  cm/s at this location. The head of the jet, as marked by the location of the fuel-ash boundary, moves inward at a fraction of the sound speed so that the size of the compressed region grows with time. Trailing behind the fuel-ash boundary is a shock wave which separates the low density, high velocity flow produced in the collision region from the compression wave which moves ahead of it. It is the ram pressure of this high velocity flow which drives the compression wave into the star. The ram pressure of this high velocity flow is balanced by the gas pressure of the compressed, overlying material, as shown by the red line in the bottom panels of Figure 4. In all of the models studied, the inward directed jet continues to compress material, heating it to carbon burning conditions until a detonation arises

and disrupt the star.

An important question in the context of the present study concerns the extent to which the jet-like flows which develop depend upon the 2D geometry used. Simulations of off-center ignition using 3D grids have been made (e.g. Röpke et al. 2007a; Jordan et al. 2008) with the general conclusions that focusing of surface flow also occurs in 3D and is not strongly diminished compared to 2D. As a point of direct comparison, we have simulated a 3D model from flame ignition through detonation using the same methods as used in the 2D models presented here. This 3D model used a finest resolution of  $\Delta=8$  km and was ignited by a 16 km flame bubble displaced 80 km from the stellar center. The development of the collision region and the subsequent detonation in the 3D model is remarkably similar to that found in the 2D models. For comparison, the profile of the jet formed in the 3D model just prior to detonation is included in the right panel of Figure 4.

Jet formation within a converging flow and jet penetration are well studied phenomena. For instance, engineers have designed shaped charge explosives which create jets by explosively collapsing a convex “liner” material, most often cone-shaped, onto itself (e.g. Birkhoff et al. 1948).<sup>2</sup> The jets thus formed have notoriously strong penetrative power and can slice and penetrate sheets of steel which are several times thicker than the shaped charge diameter and are applied in both military and industrial capacities including metal perforation, armor penetration, and oil well drilling. While there are many differences between shaped charge jet formation and the collision region flows present in our calculations, the phenomena bear interesting similarities which may provide insight into the depth to which a converging surface flow may penetrate the underlying carbon-oxygen rich layers of a white dwarf. The jet models which have been made to interpret experimental results estimate penetration depth by balancing the ram pressure of the jet material with that of the target material in a frame of reference that is moving with the jet-target interface. The penetration depth under the simplifying circumstances of constant density jet and target materials depend on only the density ratio and the jet length. This picture is greatly complicated in the stellar surface flow case where compressibility plays a central role and the pressure balance at the jet-star interface is between the dynamical pressure of the jet and the gas pressure of the core. While it is beyond the scope of the present paper to fully analyze the problem of compressible jet formation and penetration, we conclude by noting that the strong penetrative power observed in shaped charge jets provides support for the deep penetration seen in all of the simulations in our study which develop collision regions. In all of the cases which we study, the jets which have formed penetrate into denser layers of the white dwarf until a detonation occurs.

*Detonation Initiation.* — Once the density of the material undergoing carbon burning in the jet exceeds  $\rho_{\text{det}} \sim 10^7$  g/cm<sup>3</sup> a detonation initiates which then propagates away from the head of the jet at the Chapman-Jouguet speed,  $D_{CJ} \sim 1.2 \times 10^9$  cm/s with Mach number  $M = D_{CJ}/c_s \sim 3.4$ . The time sequence shown in Figure 3 captures the moment when the detonation initiates at the head of the jet and begins to spread outward. Because of the weak dependence of the detonation wave speed on the upstream density, the detonation front radiates from its point of initiation nearly spherically.

The initiation of the detonation, which takes place at the fuel-ash boundary, when  $\rho \sim 10^7$  g/cm<sup>3</sup> and  $T \sim 3 \times 10^9$  K., resembles a Zel’dovich gradient mechanism (Zel’dovich et al. 1970; Khokhlov et al. 1997). Detonation initiation through this process involves a complicated interplay between burning and hydrodynamic flow that requires a coherent build up of acoustic energy by the nuclear energy release. An often cited criteria for the initiation of a detonation in the context of degenerate carbon-oxygen material is that a “critical” mass of material needs to be heated and compressed above a certain temperature and

---

<sup>2</sup>Mining engineers have employed similar methods as early as 1792.

density threshold (Arnett & Livne 1994; Niemeyer & Woosley 1997; Röpke et al. 2007a). While these studies indicate the general conditions under which detonations might readily arise, thermodynamic conditions and heated masses alone represent a gross oversimplification of the underlying initiation process which depends sensitively on the gradients of thermodynamic variables within the heated region. Since gradients play a central role, the resolution and the geometry of the flows being simulated, such as those presented here, are important considerations when investigating the potential for detonation. The suite of simulations studied in this paper use a finest zone size which is 4 km and limits the steepness of temperature gradients which can be represented in our models. And although detonations do arise in our simulations, drawing conclusions from the results of simulations alone concerning the success or failure of detonation will require investigations at significantly higher resolution than has been possible to date.

We have made some efforts to address the robustness of initiation with a suite of simulation models which employ a patch of mesh refinement over the collision region having zones as fine as 125 m. One of the principal findings of this study, which is being prepared for publication elsewhere (C. Meakin et al. in prep), is that the gradients at the head of the inward directed jet component become steeper at higher resolution which at first appears to inhibit detonation. However, the higher resolution flows develop turbulent structures within the shear layers that form at the interface between the head of the jet and the background stellar material, such as through the Kelvin-Helmholtz instability, which thicken the fuel-ash boundary to an extent that induction time gradients conducive to the spontaneous initiation of a detonation may develop after all.

#### 4.2. Propagation of the Detonation Wave over the Stellar Core

Once the detonation wave forms it propagates outward from the spot of initiation nearly spherically, and consumes the unburned carbon and oxygen remaining in the core. The time sequence in Figure 5 shows the geometry of the detonation wave as it propagates over the stellar core. The detonation wave speed is a weak function of the upstream plasma density and varies by only  $\pm 5\%$  for the conditions present in the unburned core, where  $10^7 < \rho < 10^9 \text{ g cm}^{-3}$  (see Figure 2 of Gamezo et al. 1999). The detonation wave traverses the expanded white dwarf in  $t_{\text{cross}} \sim 2r_{\text{det}}/D_{\text{CJ}} \sim 0.4 \text{ s}$  where the core size is roughly  $r_{\text{det}} \sim 2 \times 10^8 \text{ cm}$  and the detonation wave speed is  $D_{\text{CJ}} \sim 10^9 \text{ cm s}^{-1}$ .

As the detonation wave propagates it compresses upstream material prior to burning. Upstream material with a density greater than  $\sim 10^7 \text{ g cm}^{-3}$  is compressed and heated strongly enough by the shock that complete relaxation to nuclear statistical equilibrium (NSE) occurs before the rarefaction wave behind the detonation expands the material and it freezes-out (see §5). At lower upstream densities relaxation to NSE is incomplete and the ash is composed of intermediate mass elements (IMEs) such as Si, S, Ca, and Ar, i.e., the products of incomplete silicon burning (e.g. Woosley et al. 1973; Arnett 1996).

Material which is compressed to densities exceeding  $\sim 10^8 \text{ g cm}^{-3}$  in the detonation wave develops a non-negligible neutron excess through electron capture reactions. The strong density dependence of the weak reaction rates limit this neutronization to the central-most regions of the star as evident in Figure 6 which shows the spatial distribution of electron mole fraction  $Y_e$  as the detonation wave sweeps over the stellar core. As discussed in §5, the final composition of the material burned to NSE, including the fraction which is  $^{56}\text{Ni}$ , depends on the degree of neutronization.

Detonation waves are subject to transverse instabilities which influence the structure of the reaction zone and the reaction products and introduce inhomogeneities in the downstream flow (e.g., Gamezo et al. 1999; Timmes et al. 2000b; Sharpe 2001). Therefore, in order to faithfully capture in entirety the properties



of the burning in a detonation wave the reaction length scale must be resolved. An additional complication arises in modeling detonations when the density scale height in the medium through which the detonation propagates is comparable to or smaller than the reaction length. Under these conditions steady detonation wave theory cannot be applied and the resulting reactive- hydrodynamic flow remains an active field of research (Sharpe 2001). In the context of a carbon-oxygen, near Chandrasekhar-mass white dwarf ( $M_{\text{Ch}}$ ), such conditions arise when the upstream density is  $\sim 10^7 \text{ g cm}^{-3}$ . Significant deviations from a Chapman-Jouguet detonation may arise and influence the resulting intermediate mass element (IME) yield. Since IMEs, such as Si and Ca, are primary observational diagnostics of the explosion mechanism underlying SNe Ia (e.g. Wang et al. 2003, 2007), these uncertainties have important implications for modeling all delayed detonation scenarios.

In the models presented here, the stellar cores undergo only modest expansion during the deflagration and detonation phases. Between 90% and 97% of the unburned mass in the core has a density which exceeds  $\sim 10^7 \text{ g cm}^{-3}$  at the time detonation initiates and all of this material undergoes complete relaxation to NSE, resulting in primarily  $^{56}\text{Ni}$  and a small fraction of stable Fe-peak elements (§5 and Table 1). Therefore, only a small amount of mass, which is confined to a thin shell in the outer part of the core, is burned to IMEs by the detonation wave. Within this narrow shell the length scales associated with transverse instabilities exceed the grid scale used ( $\Delta = 4 \text{ km}$ ) (Gamezo et al. 1999) and our numerical methods are sufficient to capture them. However, material in this narrow region undergoes rapid expansion after the detonation wave passes and it quickly mixes with the turbulent layer of deflagration ash which lies immediately above it so that it is difficult to discern the presence of cellular structure if it did indeed arise. Significantly higher fidelity simulations are required in order to study the impact that transverse instabilities have under these conditions. While these affects are negligible in the present suite of models, more expanded, lower density cores are likely to be much more strongly impacted by this uncertain physics.

Upon encountering the deflagration ash which enshrouds the star, the detonation wave transitions into a shock wave which accelerates the hot ash. After the detonation wave and the ensuing shock have propagated off of the computational grid, what is left behind is a rapidly expanding remnant consisting of a smoothly layered core of material burned to NSE with a thin shell of IMEs outside of that, surrounded by a turbulent layer of ash from the deflagration composed of both NSE and IME material.

#### 4.3. Transition to Free Expansion and Final Remnant Shape

As the detonation wave traverses the stellar core it shifts the density distribution so that the peak in density is initially moved in the positive  $y$ -direction. This can be seen in Figure 7 which presents a time series of velocity and density profiles spanning the time interval over which the detonation wave traverses the stellar core. The initial shift in the density peak towards positive  $y$  is due to the strong rarefaction which follows the detonation wave and expands the material behind it on a very short timescale ( $\tau_{\text{expand}} \sim 0.4 \text{ s}$ ). Within  $\sim 1 \text{ s}$  following the passage of the detonation over the core, the density peak moves back in the negative  $y$ -direction and ends up south of the equator (negative  $y$ ). The binding energy released in the detonation wave is converted into the kinetic energy associated with expansion within  $\sim 1 \text{ s}$  after the detonation wave completes its passage over the star. The total energy budget is shown in Figure 8 for the model ignited 25 km off center. By  $t \sim 4 \text{ s}$  the remnant is transitioning into a state of free expansion and assumes a self-similar shape which is no longer changing with time and the radial velocity is well described by a linear dependence on the distance from the center of the remnant. Axial and equatorial profiles of density and radial velocity in the remnant are presented in Figures 9 for two models which span the explosion outcomes in our study.

Shown in Figure 10 is the late time ( $t > 4$  s) remnant shape presented as a series of logarithmically spaced density contours for the same two models in Figure 9. What can be seen in this figure is that the asymmetry imparted by the off-center ignition and surface detonation manifests as a shift in the center of density contours even though each individual contour is well described by a circle. The overall shape of the density distribution, therefore, can be characterized by the radius  $R_c$  and center  $y_c$  of the circles which best describe each density contour. This information is shown in Figure 11. The degree to which these two curves ( $R_c$  and  $y_c$ ) approximate the remnant is shown by the thin line in Figure 9, which is the function  $r(\rho) = y_c(\rho) \pm R_c(\rho)$ .

Superimposed over the relatively smooth overall shape of the final remnant are smaller scale density inhomogeneities due to the turbulent flow associated with the deflagration and the surface flow which preceded detonation. These perturbations are quantified in the bottom panel of Figure 11 as root mean square (rms) deviations in density taken along the best fit circle at each density. The general trend is that more expanded stellar cores have larger density perturbations in their surface layers at the time of detonation. This can be accounted for partly by the fact that more expansion results from a larger amount of energy liberated in the deflagration which goes into powering the surface flow. Additionally, more expanded cores are less stably stratified at their surfaces (lower gravity and shallower pressure gradients) and so are more easily perturbed by the surface flow which passes over the star before detonation.

## 5. NUCLEOSYNTHESIS

The nucleosynthetic yield for the type of explosion model studied in this paper consist of a mixture of ash due to both a deflagration and a detonation. The total amount of the star burned in the deflagration amounts to less than  $\sim 0.1 M_\odot$  with nearly the entire remaining mass of the star consumed by the detonation wave which follows. The progress variables described in §2 which are used to parameterize the compositional evolution and energy release due to nuclear burning allow us to calculate the bulk yield of IMEs and NSE material directly from the multi-dimensional simulation data by performing simple sums (Calder et al. 2007; Townsley et al. 2007). In Table 1 the total mass burned in the deflagration  $M_{\text{def}}$  and the detonation  $M_{\text{det}}$  is summarized, including the budget of IME and NSE material. The deflagration, propagated with the ADR flame model (§2), produces a total yield which is approximately one third IMEs and two thirds NSE material, while more than 90% of the material burned in the detonation is completely relaxed to NSE.

A general feature of these explosion models is that higher density cores at the time of detonation produce a larger yield of NSE material and a smaller yield of IMEs. This trend is summarized in Figure 12 which relates the final NSE yield to the central density of the white dwarf at the time of detonation. The total mass of material having a density exceeding  $\rho = 10^7$  g/cm<sup>3</sup> is also shown as a function of central density, and provides a good measure of the mass of material that will burn to NSE in the detonation. The relationship between the amount of mass above a certain density and the central density is a property of the initial white dwarf density structure and the wave form of the pulsation which is excited in the star by the deflagration. The dashed line in Figure 12 shows the relationship expected if the pulsation is described by the fundamental mode of the linear wave equation. This mode fits the simulation data remarkably well considering how large (and non-linear) the pulsation amplitude is for the low central density end of the figure. But this can be understood by the fact that the fundamental mode is close to homologous, i.e., the displacement is nearly directly proportional to the radius of the white dwarf.

The data for the 3D model described in §4.1 has been included in Figure 12 for comparison, and shows

that the overall character of the expansion driven by the deflagration is not dimensionality dependent, nor is the nucleosynthesis that takes place in the detonation. Data from an additional 3D simulation which burned significantly more mass in the deflagration is shown and labeled “3D Multi”. This simulation data, which is part of an extended suite of 3D models investigating the mapping of ignition conditions to final explosion energies and nucleosynthetic yields (G. C. Jordan IV et al., in prep), was ignited by a uniform distribution of 30 flame bubbles enclosed in an 80 km radius sphere having its center displaced 100 km from the stellar center. This distribution of ignition points is intended to be more representative than single-point ignition of the non-axisymmetric conditions created by the interaction of the growing bubble with the pre-ignition convective core. This model demonstrates that fundamental mode radial pulsation is a good description of the core dynamics preceding detonation even for significant degrees of expansion. This model also demonstrates that off-center deflagration models are capable of producing a broad range of NSE and  $^{56}\text{Ni}$  masses, and not just the most luminous SNe Ia events.

### 5.1. Iron Peak Freeze-Out Yields: Method

As NSE material expands and cools in the rarefaction that follows the detonation wave, nuclear reactions eventually cease, the composition no longer changes and the material is said to have gone through *freeze-out*. In this section we describe a methodology to efficiently and accurately calculate iron peak yields for material which burns to NSE and then freezes out in the expansion following the detonation wave. In our hydrodynamic simulations  $\sim 10^5$  to  $\sim 10^6$  Lagrangian tracer particles are passively advected through the computational domain with an initial distribution that evenly samples the underlying mass distribution. Nucleosynthetic yields can then be calculated by integrating nuclear reaction networks along each of these particle trajectories and then summing the yields. However, when the large number of particle trajectories required for accurate yield estimates is multiplied by the number of simulation models desired for study, the computational cost of this brute force method of post-processing becomes prohibitively expensive. Therefore, we have developed an alternative approach to calculate the final composition of material processed by the detonation, which takes advantage of the fact that the final nucleosynthetic yield  $X_{i,f}$  of material burned to NSE depends only on the final entropy  $S_f$ , expansion timescale  $\tau$ , and degree of neutronization  $\eta_f$  of the detonated material to a high degree of precision with  $X_{i,f} = X_{i,f}(S_f, \eta_f, \tau)$ .

#### 5.1.1. Individual Trajectories

The temperature and density of a generic tracer particle processed by the detonation is presented in Figure 13. The evolution of  $Y_e$  and the abundances of nuclei along this trajectory have been calculated using a nuclear reaction network initialized with the initial composition of the white dwarf material in the simulation, equal mass fractions of  $^{12}\text{C}$  and  $^{16}\text{O}$ . The network code used for the integrations is a version of the network used in Calder et al. (2007) expanded to 443 nuclear species (see Table 2). The thermonuclear reaction rates are taken from an expanded version (Schatz 2005, private communication) of the rate compilation REACLIB (Thielemann et al. 1986; Rauscher & Thielemann 2000). We have also included the temperature-dependent nuclear partition functions provided by Rauscher & Thielemann (2000), both in the determination of the rates of inverse reactions and in our determination of NSE abundance patterns. Electron screening of thermonuclear reaction rates is incorporated, adopting the relations for weak screening and strong screening provided by Wallace et al. (1982) (for additional details see the appendix of Calder et al. 2007). Contributions from weak reactions are included using the rates provided by Langanke & Martínez-Pinedo (2001).

The time evolution during the rarefaction stage of several abundant species along this trajectory, parameterized by plasma temperature, is shown in Figure 14 (solid lines). The NSE composition corresponding to the same density and neutron excess for each temperature along the rarefaction part of the trajectory is also shown for comparison (dashed lines). The NSE mass fractions were determined with the NSE solver described in Calder et al. (2007) and Seitenzahl et al. (2008a), which uses the same nuclear physics as the reaction network code. Figure 14 illustrates the degree to which adopting an NSE state at a particular “freeze out temperature” is a poor approximation to the final freeze-out abundances. This is true because nuclei freeze-out over a fairly large range in temperature and there is non-trivial evolution in a nuclide’s abundance after it falls out of NSE but before it reaches its asymptotic freeze-out value.

The thermodynamic trajectories for Lagrangian elements (i.e., tracer particles) processed by the detonation wave are well characterized by an exponential temperature evolution

$$T(t) = T_0 \exp(-t/\tau) \quad (1)$$

and a corresponding density evolution found by assuming adiabaticity

$$S(t) = S(T, \rho, \bar{A}, \bar{Z}) = S_f = (\text{constant}) \quad (2)$$

where  $S_f$  is the final entropy in the post-detonation state and  $\bar{A}$  and  $\bar{Z}$  are the average atomic weight and charge of the plasma during the burn with  $Y_e = \bar{Z}/\bar{A}$ . The density in equation 2 is found using the same Helmholtz equation of state (Timmes & Arnett 1999; Timmes & Swesty 2000a; Fryxell et al. 2000) used in the hydrodynamic simulations. A parameterized trajectory, is shown in Figure 13 for comparison to the particle trajectory.

The abundance evolution for this parameterized trajectory is presented in Figure 14 (dotted line) and shows agreement to a high degree of precision with the tracer particle trajectory. Because the composition is well described by a NSE distribution at temperatures above  $T_9 \sim 5.5$  the final yields are not dependent on the peak temperature reached by the particle trajectory and depend only on the entropy, the total amount of neutronization, and the expansion timescale. Final asymptotic freeze-out yields are safely adopted when the plasma temperature drops below  $T \sim 10^9$  K with no evolution in the abundances taking place at lower temperatures. Because the electron capture rates are a strong function of density, neutronization occurs in the short lived high density region formed immediately behind the detonation front, while the material is still in NSE and well before freeze-out begins.

### 5.1.2. Systematic Properties of the Post-Detonation State and Generating a Lookup Table

A tight correlation between the degree of neutronization  $\eta_f$  and the final entropy  $S_f$  of the detonated material further simplifies the procedure and allows us to calculate the final composition for each grid zone in our simulations using a one parameter freeze-out abundance lookup table  $X_{i,f} = X_{i,f}(\eta_f)$ . The asymptotic values of the degree of neutronization  $\eta_f = (1 - 2Y_{e,f})$  and the entropy  $S_f$  for all of the stellar matter burned into NSE in the detonation wave is found to lie along a narrow ridge in the  $S_f$ - $\eta_f$  plane as shown in Figure 15. This correlation arises from the monotonic dependence of the entropy deposition and the neutronization rate  $\dot{Y}_e(\rho)$  on the post-shock plasma density in the detonation wave (which is itself a monotonic function of the pre-shocked, upstream density). (Note, this tight correlation doesn’t exist for the material which is

burned in the deflagration so that the method described here is not applied to that phase of burning.)

A lookup table is constructed along the black line shown in Figure 15 and has been sampled at 50 locations logarithmically spaced in neutron excess  $\eta$ . For every value of  $\eta$  in the table, the freeze-out abundances are calculated by integrating the nuclear reaction network, with weak interactions turned off, over an adiabatic analytic trajectories as described above for the corresponding value of  $S_f$ . The network is initialized with NSE composition at  $T_9 = 6.0$  and the integration continued until  $T_9 < 1.0$ , at which time freeze-out has occurred. A summary of the stable iron peak yields for material along this locus of points is presented in Figure 17. The freeze-out abundances for a computational zone are then be found by using the table entry with the corresponding value of  $\eta$ . The table lookup is computationally fast, and once the table is created no additional network calculations are necessary.

As described above, the final freezeout yield depends on the expansion timescale  $\tau$ . The expansion timescale, defined by eq.[1] and found by fitting an exponential to the temperature histories of the tracer particles, varies smoothly across the face of the white dwarf in the narrow range  $0.2 < \tau < 0.6$  s for all of the models simulated (the range is narrower for an individual explosion model). If one wanted to incorporate this information into the processing of the final yields, the range in expansion timescales would need to be reflected in the network calculations. In the work presented here, we adopt a central value of  $\tau = 0.4$  s and we discuss the sensitivity of the final yields to variations in this value in §5.2 below.

## 5.2. Iron Peak Freeze-Out Yields: Results

We calculate the final yield of stable iron peak isotopes for all of our explosion models using the procedure outlined in §5.1 above. In Figure 18 we present yields for isotopes in the mass range  $A = 45$  to  $68$  ( $^{45}\text{Ti}$  to  $^{68}\text{Zn}$ ), accounting for the decay of radioactive isotopes. The yields ( $X_i$ ) are scaled to the  $^{56}\text{Fe}$  abundance ( $X_{Fe}$ , from the decay chain  $^{56}\text{Ni} \rightarrow ^{56}\text{Co} \rightarrow ^{56}\text{Fe}$ ) and the corresponding relative solar system ratio ( $X_{i,\odot}/X_{Fe,\odot}$ ) based on the abundances of Lodders (2003). In Table 3 we present the elemental abundances for the iron peak elements from Ti to Zn scaled to Fe and solar system ratios. In all cases we highlight results for three explosion models which bracket the range of initial conditions and final outcomes found in our simulation suite. In addition, we provide a detailed list of the final integrated iron peak yields in units of solar mass in Table 4, including the abundances of radioactive isotopes and their half lives. This table can be used to determine the absolute yield of a particular isotope, or to examine the isotopic ratios of specific elements of interest.

The iron peak yields are similar to pure deflagration models such as the one-dimensional model of Nomoto (W7 yields in Brachwitz et al. 2000) and the three dimensional model presented in Travaglio et al. (2004). The iron peak yield for the pure deflagration models are more neutron rich than our models, however, because of the higher densities under which the deflagration burns material to NSE. The highest density core to detonate in our model suite (with  $r_{\text{off}}=100$  km) neutronized the most in the detonation and bears the most similarity to a pure deflagration model in terms of integrated yields. The most neutron-rich isotopes of each element (e.g.  $^{50}\text{Ti}$ ,  $^{54}\text{Cr}$ ,  $^{58}\text{Fe}$ ) have no appreciable contribution from the NSE material created by the detonation. There is likely some of these species in the small amount of deflagration material not included in our post-processing. Notably, none of our models produce untoward overabundances ( $\gtrsim 2$  times solar, indicated by the dotted lines) of either  $^{54}\text{Fe}$  or  $^{58}\text{Ni}$ . Overproduction of these nuclides continues to be a serious shortcoming of deflagration models, both spherical and multi-dimensional, which process much of the stellar interior to NSE before expansion can occur. The spatial distribution of the material in

our detonation models, however, remains layered in space and velocity while the burning products in the pure deflagration model are strongly mixed due to the turbulent nature under which burning proceeds in a deflagration (e.g. Röpke et al. 2007b; Gamezo et al. 2003).

Interestingly, the total yield of  $^{56}\text{Ni}$  in all of the explosion models presented here is  $\sim 1.1M_{\odot}$  independent of the degree of expansion which takes place prior to detonation. This is due to a self regulating process comprised of pre-expansion and neutronization which counteract each other. While the total yield of material burned to NSE is larger for stars which detonate at higher central densities, more neutronization takes place which shifts the iron peak yield to more neutron rich isotopes and away from  $^{56}\text{Ni}$  (see e.g. Timmes et al. 2003). The highest density core at detonation produces overall more stable iron peak isotopes but approximately the same  $^{56}\text{Ni}$  yield as the core with the lowest density at detonation. It can be seen from Figure 12, however, that this trend cannot hold for significantly more expanded cores since the total mass of high density material drops off precipitously as lower central densities are reached and will therefore result in SNe Ia explosions which have smaller  $^{56}\text{Ni}$  yields.

*Dependence on progenitor neutronization.* — The progenitor white dwarf model used in our explosion calculations is composed of equal parts  $^{12}\text{C}$  and  $^{16}\text{O}$  so that  $Y_e = 0.5$  everywhere in the unburned fuel prior to detonation. However, the progenitor is expected to develop a neutron excess before flame ignition both during the CNO and He burning cycles and during a  $\sim 1000$  yr epoch of hydrostatic carbon burning which is sometimes referred to as “simmering”. Recent studies of the “simmering” epoch indicate that when carbon burning runs away locally and a flame is born,  $\eta^{\text{sim}} \approx 10^{-3}$  (Piro & Bildsten 2008; Chamulak et al. 2008), while stars with an initial metallicity comparable to solar will develop a neutron excess of  $\eta_{\odot} \approx 1.5 \times 10^{-3}$  by the time core He burning commences.

The neutronization which takes place during the detonation is restricted to the densest, central-most regions of the stellar core because of the strong density dependence of the electron capture rates (see Figure 6). The resulting distribution of neutronization is presented in Figure 16. This distribution extends to values lower than the minimum  $\eta_{\text{min}}^{\text{sim}}$  expected in the progenitor prior to explosive burning. We explore the impact that such a neutronization floor will have on the yields by enforcing  $\eta = \max(\eta_{\text{min}}, \eta)$  prior to calculating the iron peak yields using the lookup table method described in §5.1. The results are presented in Figure 18 (right panel) which shows yields calculated after applying neutronization floors of  $\eta_{\text{min}} = 0$ ,  $10^{-3}$ , and  $2 \times 10^{-3}$  for the model which was least neutronized during the detonation (with  $r_{\text{off}} = 25$  km), and therefore has the most mass affected by a floor in  $\eta$ . The iron peak elements which are primarily produced at low  $\eta$  and are therefore most strongly affected by a neutronization floor are V, Cr, Mn, and Zn, although the isotopic ratios across the entire iron peak are affected.

*Sensitivity to scatter in  $S_f$  and  $\tau$ .* — It is possible to construct a higher dimensional lookup table for calculating yields which accounts for the scatter about the  $\eta$ - $S_f$  curve used to generate the table (Figure 15), but the total error associated with neglecting this scatter in final entropy  $S_f$  is small. In Figure 19 (right) we present the total variation in the yields due to shifting the  $\eta$ - $S_f$  curve in final entropy by  $\pm 5\%$ , which is the range of the scatter. Similarly, the freezeout timescale that takes place in the wake of the detonation wave has some scatter about the fiducial value of  $\tau = 0.4$  s that has been used for the results presented above, spanning the range  $0.2 < \tau < 0.6$  s. The total spread in yields adopting the extreme values for  $\tau$  is shown in Figure 19 (left). The variation in the yield will be significantly smaller than illustrated by these figures since there exists a smooth distribution between the extreme values of  $S_f$  and  $\tau$  with the majority of the mass peaked about the central value.

### 5.2.1. The velocity distribution of the yield.

*The yield of NSE material.* — Inferring the abundance stratification in SNe Ia is possible by studying high fidelity, multi-epoch spectra; a technique which is proving to be a powerful new tool for constraining explosions models (Stehle et al. 2005; Röpke et al. 2007b; Mazzali et al. 2008). The total number of objects which have had detailed internal abundance stratifications reconstructed to date is small (only 2 at the time of writing, including 2002bo and 2004eo). These two low luminosity SNe have inferred  $^{56}\text{Ni}$  masses in the range  $M[^{56}\text{Ni}] \sim 0.43 - 0.52 M_{\odot}$ . Despite the very different  $^{56}\text{Ni}$  masses between these two observed SNe and the explosion models presented in this paper, it is interesting to compare the qualitative and quantitative properties of the abundance stratifications in an attempt to understand the nature of and the diversity inherent in the explosion mechanism.

For the case of SN 2004eo, Stehle et al. (2005) find  $M[^{56}\text{Ni}] \sim 0.43 M_{\odot}$ . In their reconstruction, the  $^{56}\text{Ni}$  mass fraction drops below 0.5 at  $v_{\text{exp}} \sim 7,000$  km/s, and drops below 0.1 at 12,000 km/s. For the case of SN 2002bo, Mazzali et al. (2008) find  $M[^{56}\text{Ni}] \sim 0.52 M_{\odot}$ . The  $^{56}\text{Ni}$  mass fraction drops below 0.5 at  $v_{\text{exp}} \sim 10,000$  km/s and drops below 0.1 at 15,000 km/s. In both of these SNe, a high mass fraction of stable Fe ( $X_{\text{Fe}} \sim 1$ ) is inferred at low velocities  $v_{\text{exp}} < 3,000$  km/s.

The distribution of the elemental abundances as a function of the radial velocity for our explosion models is presented in Figure 20. In this figure, the elemental abundances are calculated by summing over isotopes and taking into account radioactive decays with half lives less than 1 day. Two models are shown which bracket the final outcome of all the explosions modeled in this paper. Both models produce  $\sim 1.1 M_{\odot}$  of  $^{56}\text{Ni}$ . The model ignited with  $r_{\text{off}} = 25$  km is the most expanded at the time of detonation, neutronizes the least amount in the detonation, and has the lowest explosion energy,  $E_{\text{tot}} = 1.45 \times 10^{51}$  erg. The contribution of stable Fe is the smallest in this model, having a mass fraction  $X_{\text{Fe}} \sim 10^{-3}$  out to  $v_{\text{exp}} \sim 2,000$  km/s. The mass fraction of  $^{56}\text{Ni}$  drops below 0.5 at  $v_{\text{exp}} \sim 14,000$  km/s, and drops below 0.1 at  $\sim 16,000$  km/s. The model ignited with  $r_{\text{off}} = 100$  km is the least expanded at the time of detonation, is neutronized the most by the detonation wave, and has the largest explosion energy,  $E_{\text{tot}} = 1.52 \times 10^{51}$  erg. Although the ejecta at low velocities is still dominated by  $^{56}\text{Ni}$ , stable Fe with a mass fraction exceeding  $X_{\text{Fe}} \sim 0.1$  is present out to  $v_{\text{exp}} \sim 6,000$  km/s. The mass fraction of  $^{56}\text{Ni}$  drops below 0.5 at a velocity of  $v_{\text{exp}} \sim 16,000$  km/s and drops below 0.1 at 18,500 km/s.

While the total yield of  $^{56}\text{Ni}$  is significantly larger in the explosion models presented here, the qualitative layered structure of the remnant and the near absence of unburned carbon and oxygen are in good agreement between the models and the observations. As discussed in §5 and summarized in Figure 12, lower  $^{56}\text{Ni}$  masses can be produced in surface detonation models which release more energy during the deflagration phase. However, detonations which take place at lower central densities and produce smaller  $^{56}\text{Ni}$  masses, undergo significantly less neutronization and will therefore fail to reproduce the stable Fe core which has been inferred in the two models discussed above. On the other hand, it is possible that the neutron rich region seen at low velocities in SNe Ia remnants are a vestige of the progenitor conditions at ignition. The nature of the progenitor at flame ignition, including the central density and  $Y_e$  distribution, are uncertain and will remain so until the evolution leading up to ignition is better understood, including the much debated and poorly understood Urca process (see e.g., Lesaffre et al. 2005; Arnett 1996).

*The yield of non-NSE material.* — The detailed yield for material which has not completely relaxed to NSE prior to freezeout and is composed primarily of IMEs such as Si, S, and Ca is not presented here. In addition to producing IMEs, material which has begun silicon burning but has not yet reached an NSE state will contribute to the iron peak with isotopic ratios that are very different from that which reaches an

NSE state. While the impact of this burning process is small for the suite of explosion models presented in this paper, which produce primarily NSE material, it is essential to accurately calculate the composition and distribution of this material for lower luminosity (lower  $^{56}\text{Ni}$  mass) SNe Ia explosion models which will have a significantly larger contribution of non-NSE material. Additionally, although the total contribution of IMEs to the mass of the remnant is small in all of the explosions presented here this material plays a central role in modeling the observational signatures of these explosion models and is therefore crucial for comparing our calculations to observational data. Therefore, a procedure for determining incomplete silicon burning yields which is similar to the method described in §5.1 is being developed (C. Meakin et al., in preparation).

## 6. CONCLUSIONS

We have studied the final outcomes for a range of single point flame ignition models of thermonuclear supernovae within the computational framework developed at the FLASH center (§2 and Fryxell et al. (2000); Calder et al. (2007); Townsley et al. (2007); Seitenzahl et al. (2008a)). For the first time in this work, we have extended the 3-stage reactive ash model for nuclear burning described in Townsley et al. (2007) to study the ignition and propagation of the detonation mode of burning. As a result, our explosion models are unique in terms of the degree to which non-idealized nuclear physics are employed, including a non-static, tabularized treatment of the nuclear statistical equilibrium (NSE) state and the inclusion of contemporary weak reaction rates (Seitenzahl et al. 2008a). In addition, we have demonstrated here, by reaction network post-processing of recorded Lagrangian histories, that the 3-stage reactive ash model provides a suitable reproduction of fluid density and temperature histories to allow detailed nucleosynthesis, including self-consistent neutronization. Using these techniques, we have followed the progression of a thermonuclear flame (deflagration) from a single ignition point which is varied to successively larger distances from the center of a carbon oxygen white dwarf, and we have described in detail the resulting surface flows and detonation which ensue.

Detonations arise within a colliding surface flow for all models which are ignited at a radial location which exceeds  $\sim 20$  km in our 2D simulations. Flames ignited closer to the stellar center release enough nuclear energy to significantly expand the stellar core to a degree that it stalls the surface flow, thus preventing a strong collision region and detonation. The nuclear binding energy released in these stalled surface flow models, however, is not enough to gravitationally unbind the star and they remain viable candidates for a pulsational detonation upon recollapse (Khokhlov 1991; Arnett & Livne 1994). Models which detonate release  $\sim 2 \times 10^{51}$  erg in nuclear binding energy, resulting in a supernova-like explosion with total energy  $E_{\text{tot}} \sim 1.5 \times 10^{51}$  erg.

In all of the models in our parameter study which produce supernova-like explosions, detonation initiates within a jet-like flow which forms in the converging surface flow. This is in agreement with the results presented in Kasen & Plewa (2007). However, we do not find that the detonation initiates through a shock to detonation transition (SDT) as suggested by these authors, but instead find that the detonation occurs through a gradient mechanism. The initiation of the detonation takes place within the compressed gas which lies ahead of the high velocity jet, and ahead of the internal shock which forms within the jet (see §4 and Figure 4). The focusing of the surface flow and the formation of the jet is also present in 3D simulations (§4, and Jordan et al. 2008; Röpke et al. 2007a), and is therefore not an artifact of the 2D axisymmetric geometry used.

Within a few seconds after the detonation wave disrupts the stellar core, homologous expansion is beginning to be established. By  $t \sim 4$  s from flame ignition more than 90% of the total energy is in the



kinetic energy of expansion, and the expansion velocity has acquired a linear dependence on radius. The final remnant possesses both global and small scale asymmetries which will influence the observational signature. When the remnant enters the homologous expansion phase it is characterized by a smooth, layered inner core surrounded by a low density, flocculent layer of deflagration ash which was dumped onto the surface of the star prior to detonation. The smooth inner core of the remnant has a global north-south asymmetry due to off-center ignition and surface detonation, which is well characterized by circular isodensity contours which are progressively off-center at higher densities (see § 4.3 and Figure 11).

We have analyzed in detail the nucleosynthesis of material burned to NSE in the detonation. These results have been generated from the multi-dimensional simulation data using a newly developed post-processing method which takes advantage of the uniqueness of the NSE state and systematic properties of detonation waves. The method, presented in §5, obviates the need for computationally prohibitive network calculations along each of the millions of particle trajectories which are necessary for good mass resolution in 3D explosion models. This work addresses only material which has relaxed to NSE, which forms, by mass, nearly all of the yield from the 2-dimensional explosion models of this study. Extending the method to include detailed isotopic yields for material incompletely relaxed to NSE (incomplete carbon, oxygen, and silicon burning) is being developed and will be described in a forthcoming publication (C. Meakin, in prep). Nucleosynthesis of material processed in a deflagration instead of detonation burning mode can be processed with a similarly parameterized method, though requiring more parameters, if it reaches NSE. This leaves only the relative minority of tracks in partially burned deflagration material to be processed directly (only a few percent of all the trajectories).

Larger offsets of the ignition point lead to less stellar expansion prior to detonation and therefore the production of more NSE material. However, we find that the amount of  $^{56}\text{Ni}$  produced stays roughly fixed at  $\sim 1.1M_{\odot}$  for all of our 2-dimensional explosion models which extend down to a central density of  $\rho_c \sim 4 \times 10^8 \text{ g/cm}^3$  at the time of detonation. This regulation is due to the enhanced neutronization at the higher densities characteristic of the less-expanded cases. Higher density cores at the time of detonation result in more neutronization, and therefore a larger fractional yield of stable Fe-peak isotopes (e.g.,  $^{54}\text{Fe}$  and  $^{58}\text{Fe}$ ). The isotopic distribution we find in the Fe-peak is very similar to that found for pure deflagration models, but is characterized by a lower degree of neutronization. Less neutronization is a result of the lower densities under which the burning proceeds in our surface detonation models compared to pure deflagrations, due to the pre-detonation expansion. Between 0.06 and  $0.14M_{\odot}$  of intermediate mass elements are produced at high velocities. Regions in which more than half of the mass is in the form of IMEs lie above an expansion velocity of 14,000 km/s for all of the 2-dimensional detonation models calculated.

We successfully reproduced the relationship between the central density and mass-density distribution in the pre-detonation expanded star by superposing on the hydrostatic star the lowest order radial mode calculated in a linear approximation. We find that much smaller  $^{56}\text{Ni}$  yields are expected in cores which undergo more expansion prior to detonation (see Figure 12). This degree of expansion appears to be achievable in 3-dimensional simulations which relax the constraints on axisymmetry of the ignition conditions necessary for 2-dimensional simulations. Thus it is expected that more realistic simulations, which include the pre-ignition convection field and its effect on the growing flame bubble, will be characterized by such larger expansions. However, further analysis of such simulations, which will be the subject of future papers, is required.

Future work on elucidating the SNe Ia explosion mechanism which is being pursued at the FLASH center involves the following. (1) We are extending our survey of the mapping between flame ignition conditions and final outcomes within the computational framework developed at the FLASH center, including multi-point

ignition conditions and 3D models. (2) A simulation pipeline is being constructed to generate synthetic observational diagnostics for the explosion models, including light curves and spectra, which will allow a more direct comparison between the systematic properties of the single degenerate Type Ia model and observational data.

We thank Snezhana Abarzhi for bringing to our attention the literature on cumulative jets and shaped charges. We also thank Fang Peng for making her nuclear reaction network code available to us for this work. This work is supported in part at the University of Chicago by the Department of Energy under Grant B523820 to the ASC/Alliances Center for Astrophysical Thermonuclear Flashes, and the National Science Foundation under Grant PHY 02-16783 for the Frontier Center “Joint Institute for Nuclear Astrophysics” (JINA), and at the Argonne National Laboratory by the U.S. Department of Energy, Office of Nuclear Physics, under contract DE-AC02-06CH11357.

## A. FREEZE OUT ABUNDANCES: DETAILED IRON PEAK YIELDS

The iron peak nucleosynthetic yields for three models spanning the range of ignition conditions simulated are summarized in Table 4. The isotopes presented have been selected based on a limiting abundance ( $M_{i;0,f} > 10^{-20} M_{\odot}$ ). Two columns are shown for each model including the initial yield and the final yield after radioactive decays have been taken into account. The half lives and decay modes are presented for unstable isotopes.

## REFERENCES

- Arnett, D. 1996, *Supernovae and Nucleosynthesis: An Investigation of the History of Matter, from the Big Bang to the Present*, by D. Arnett. Princeton: Princeton University Press, 1996.,
- Arnett, D., & Livne, E. 1994, *ApJ*, 427, 315
- Birkhoff, G., MacDougall, D. P., Pugh, E. M., & Taylor, G. 1948, *Journal of Applied Physics*, 19, 563
- Brachwitz, F., et al., 2000, *ApJ*, 536, 934
- Branch, D., Livio, M., Yungelson, L. R., Boffi, F. R., & Baron, E. 1995, *PASP*, 107, 1019
- Calder, A.C., et al, 2007 *ApJ* 656, 313C
- Caughlan, G. R., & Fowler, W. A. 1988, *Atomic Data and Nuclear Data Tables*, 40, 283
- Chabrier, G., Potekhin, A., 1998, *Phys. Rev. E*, 58, 4941
- Chamulak, D. A., Brown, E. F., Timmes, F. X., & Dupczak, K. 2008, *ArXiv e-prints*, 801, arXiv:0801.1643
- Colella, P., & Glaz, H. M. 1985, *Journal of Computational Physics*, 59, 264
- Colella, P., & Woodward, P. R. 1984, *Journal of Computational Physics*, 54, 174
- Dursi, L. J., & Timmes, F. X. 2006, *ApJ*, 641, 1071
- Fryxell, B., Mueller, W., & Arnett, D., MPIA technical report

- Fryxell, B., et al. 2000, ApJS, 131, 273
- Gamezo, V. N., Wheeler, J. C., Khokhlov, A. M., & Oran, E. S. 1999, ApJ, 512, 827
- Gamezo, V. N., Khokhlov, A. M., Oran, E. S., Chtchelkanova, A. Y., & Rosenberg, R. O. 2003, Science, 299, 77
- Gamezo, V. N., Khokhlov, A. M., & Oran, E. S. 2005, ApJ, 623, 337
- Hillebrandt, W., & Niemeyer, J. C. 2000, ARA&A, 38, 191
- Jordan, G. I., Fisher, R., Townsley, D., Calder, A., Graziani, C., Asida, S., Lamb, D., & Truran, J. 2007, ApJ, 681, 1448
- Kasen, D., & Plewa, T. 2007, ApJ, 662, 459
- Khokhlov, A. M. 1991, A&A, 245, 114
- Khokhlov, A. M. 1995, ApJ, 449, 695
- Khokhlov, A. M., Oran, E. S., & Wheeler, J. C. 1997, ApJ, 478, 678
- Langanke, K., Martínez-Pinedo, G., 2001, ADNDT, 79, 1
- Lee, J.H.S., & Higgins, A.J. 1999. Phil. Trans. R. Soc. Lond. A 357, 3503
- Lesaffre, P., Podsiadlowski, P., & Tout, C. A. 2005, Nuclear Physics A, 758, 463
- Lodders, K. 2003, ApJ, 591, 1220
- Mazzali, P. A., Sauer, D. N., Pastorello, A., Benetti, S., & Hillebrandt, W. 2008, MNRAS, 456
- Niemeyer, J. C., & Woosley, S. E. 1997, ApJ, 475, 740
- Nomoto, K., Thielemann, F.K., Yokoi, K, 1984, ApJ, 286, 644
- Piro, A. L., & Bildsten, L. 2008, ApJ, 673, 1009
- Plewa, T. 2007, ApJ, 657, 942
- Rauscher, T., Thielmann, F.-K., 2000, ADNDT, 75, 1R
- Riess, A. G., et al. 1998, AJ, 116, 1009
- Röpke, F. K., Woosley, S. E., & Hillebrandt, W. 2007, ApJ, 660, 1344
- Röpke, F. K., Hillebrandt, W., Schmidt, W., Niemeyer, J. C., Blinnikov, S. I., & Mazzali, P. A. 2007, ApJ, 668, 1132
- Schmidt, W., Niemeyer, J. C., & Hillebrandt, W. 2006, A&A, 450, 265
- Schmidt, W., Niemeyer, J. C., Hillebrandt, W., Röpke, F. K. 2006, A&A, 450, 283
- Seitenzahl, I., Townsley, D., Peng, F., Truran, J., ADNDT, in press.
- Seitenzahl, I., et al., in preparation.

- Sharpe, Gary J., 2001, MNRAS, 322, 614
- Stehle, M., Mazzali, P. A., Benetti, S., & Hillebrandt, W. 2005, MNRAS, 360, 1231
- Thielemann, F.-K., Truran, J., Arnould, M., 1986, Advances in Nuclear Astrophysics, ed. E. Vangioni-Flam et al. (Gif-sur-Yvette: Editions Frontières), 525
- Timmes, F. X., Arnett, D., 1999, ApJS, 125, 277
- Timmes, F. X., Brown, E. F., & Truran, J. W. 2003, ApJ, 590, L83
- Timmes, F. X., & Swesty, F. D. 2000, ApJS, 126, 501
- Timmes, F. X., et al. 2000, ApJ, 543, 938
- Timmes, F. X., & Woosley, S. E. 1992, ApJ, 396, 649
- Travaglio, C., et al., 2004, A&A, 425, 1029
- Townsley, D., et al., 2007, ApJ, submitted
- Wallace, R., Woosley, S., Weaver, T., 1982, ApJ, 225, 1021
- Wang, L., et al. 2003, ApJ, 591, 1110
- Wang, L., Baade, D., & Patat, F. 2007, Science, 315, 212
- Woosley, S. E., Arnett, W. D., & Clayton, D. D. 1973, ApJS, 26, 231
- Woosley, S. E., Wunsch, S., & Kuhlen, M. 2004, ApJ, 607, 921
- Zel'dovich, Ya. B., Librovich, V. B., Makhviladze, G. M., & Sivashinsky, G. I. 1970, Acta Astron., 15, 313

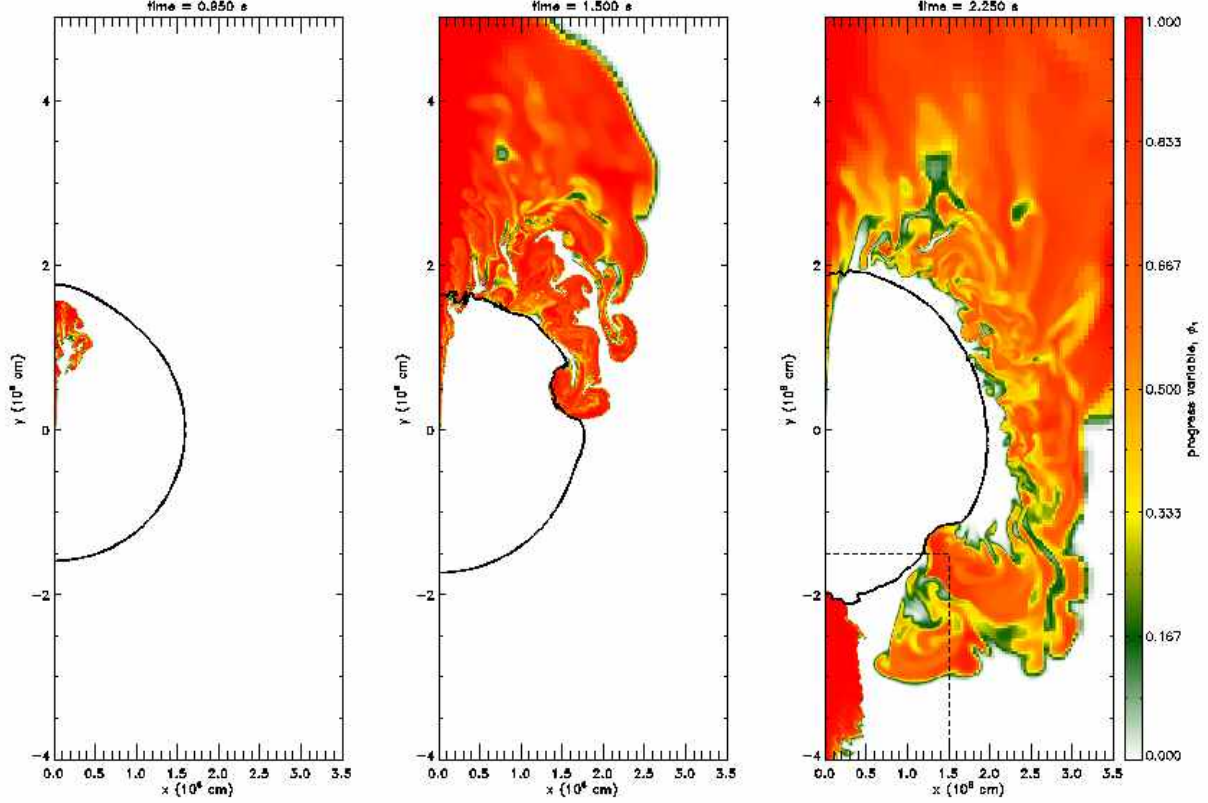


Fig. 1.— This time sequence of ash abundance (represented by the  $\phi_1$  progress variable) shows how a bubble ignited near the stellar core rises buoyantly, erupts from the star’s surface and drives a flow which is largely confined to the surface of the star by gravity. The black contour line indicates a density of  $10^7 \text{ g cm}^{-3}$ . Eventually the surface flow converges at the opposite pole from the breakout location, compressing material in that region until it begins to burn carbon. The dashed box in the right panel indicates the region detailed in Figure 3 below, where the converging flow produces a jet that initiates a detonation wave.

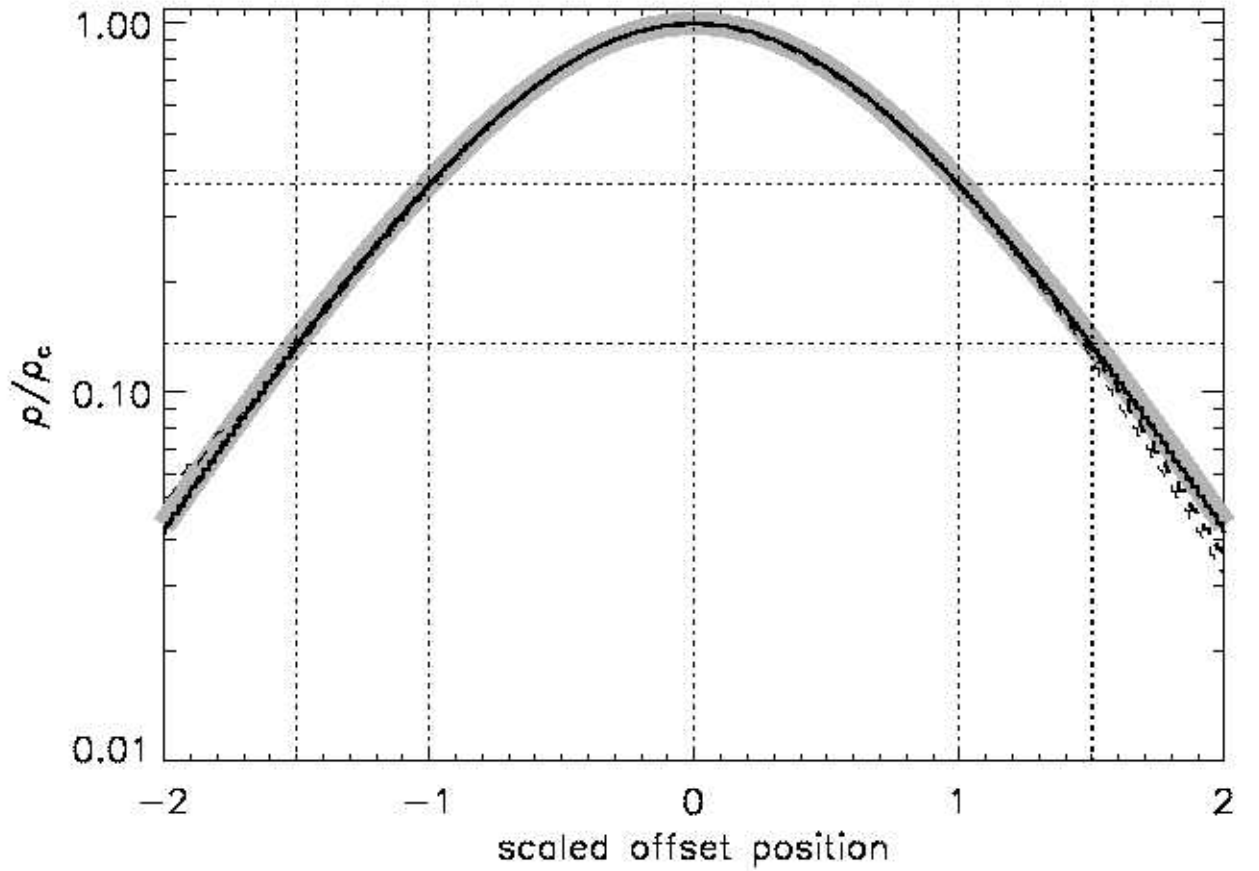


Fig. 2.— The radial density profile scaled to the central density and the density e-folding height for the initial white dwarf (thick grey line), and at the time when a surface detonation initiates ( $t_{\text{det}}$ , see Table 1) for flame bubbles ignited at 25 (thin black lines) and 100 km (thick black lines) off-center. Equatorial (solid lines) and polar (dashed lines) profiles are shown for both of the pre-detonation models and are well described by homologous expansion with minimal asymmetry.

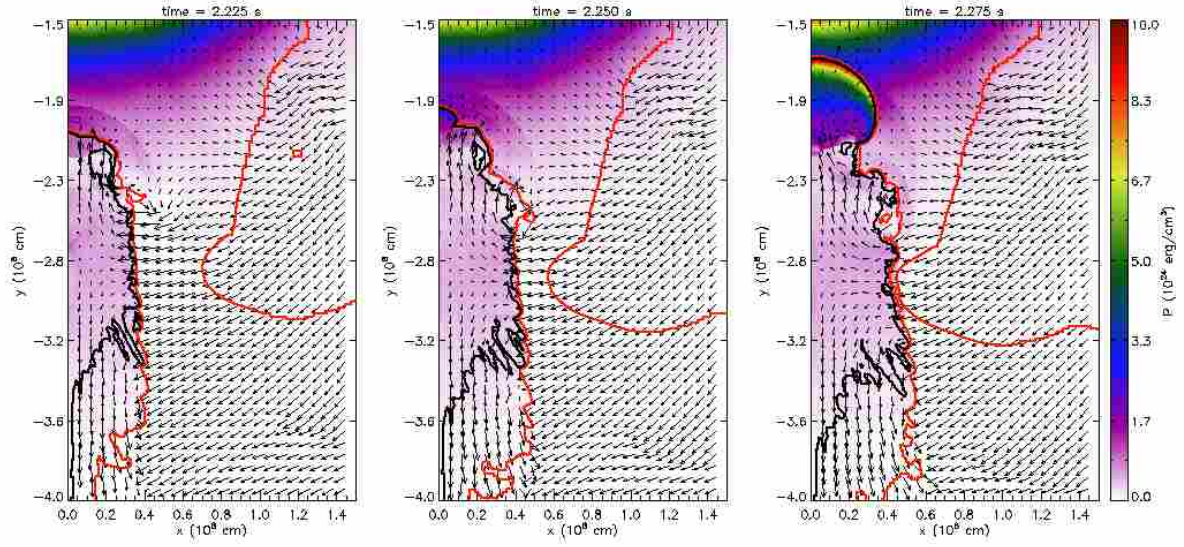


Fig. 3.— A time sequence showing the “collision region” and the bidirectional jet-like flow for the model ignited 40 km off-center. The pressure field and the velocity field are shown as the detonation wave initiates and begins to break away from the end of the inwardly moving jet component. The red and black contour lines indicate carbon depletion at the 1% and 99% levels, respectively. In the region where the detonation initiates the density and temperature are  $10^7$  g/cm<sup>3</sup> and  $4 \times 10^9$  K. The longest velocity vector indicates a flow speed of  $v_{\text{vec}} = 10^9$  cm/s, while other vectors have lengths linearly proportional to the flow speed.

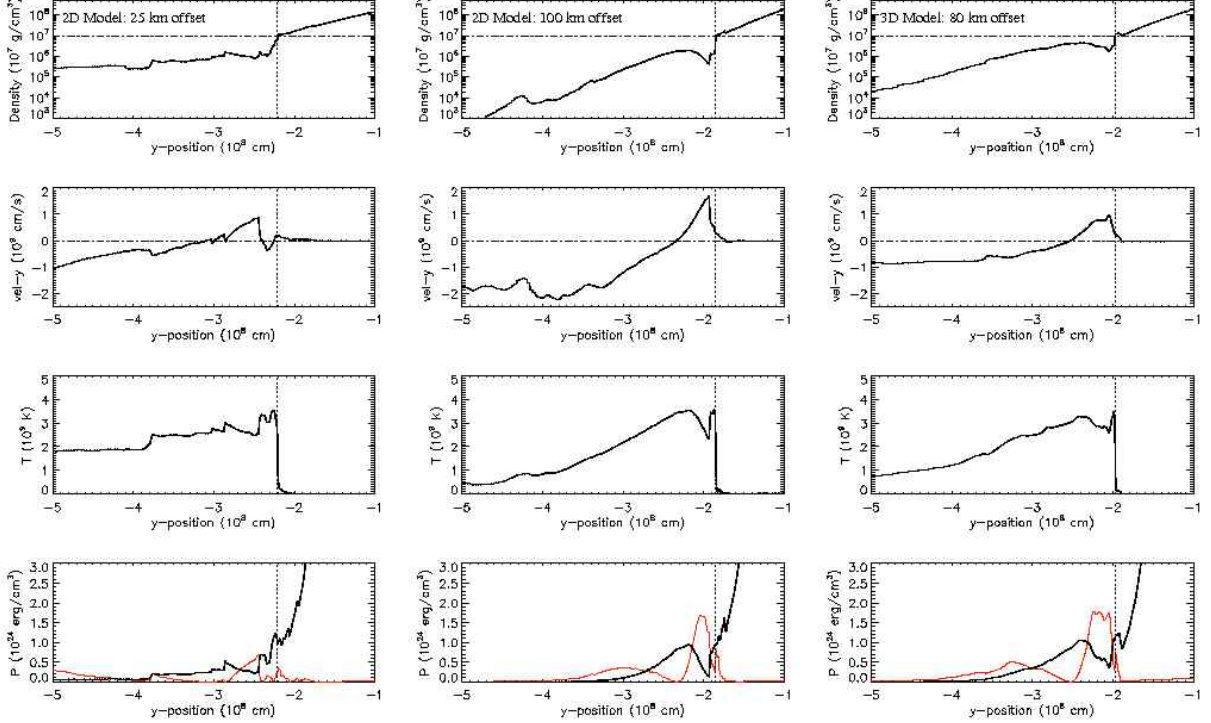


Fig. 4.— Flow properties along the jet axis prior to detonation for 2D and 3D models, including density, radial velocity, temperature, and gas pressure. The radially directed ram pressure,  $p_{\text{ram}} = \rho v_r^2$ , is shown in the pressure figure for each model by the thin red line. The 2D models shown were ignited by 16 km radius flame bubbles with offset (left)  $r_{\text{off}} = 25 \text{ km}$  and (middle)  $r_{\text{off}} = 100 \text{ km}$ . A low resolution ( $\Delta = 8 \text{ km}$ ) 3D model is shown (right) which was ignited by a 16 km radius flame bubble with offset  $r_{\text{off}} = 80 \text{ km}$  for comparison. The dashed vertical lines mark the locations of the burning front for each model, taken to be where  $\phi_1 = 0.5$ . In the top panel, the horizontal dot-dashed line marks a density of  $10^7 \text{ g/cm}^3$ , a value above which detonation readily arises in the simulations once it reaches a temperature of  $T \sim 2 \times 10^9 \text{ K}$ . The velocity zero point is marked by a dot-dashed horizontal line.



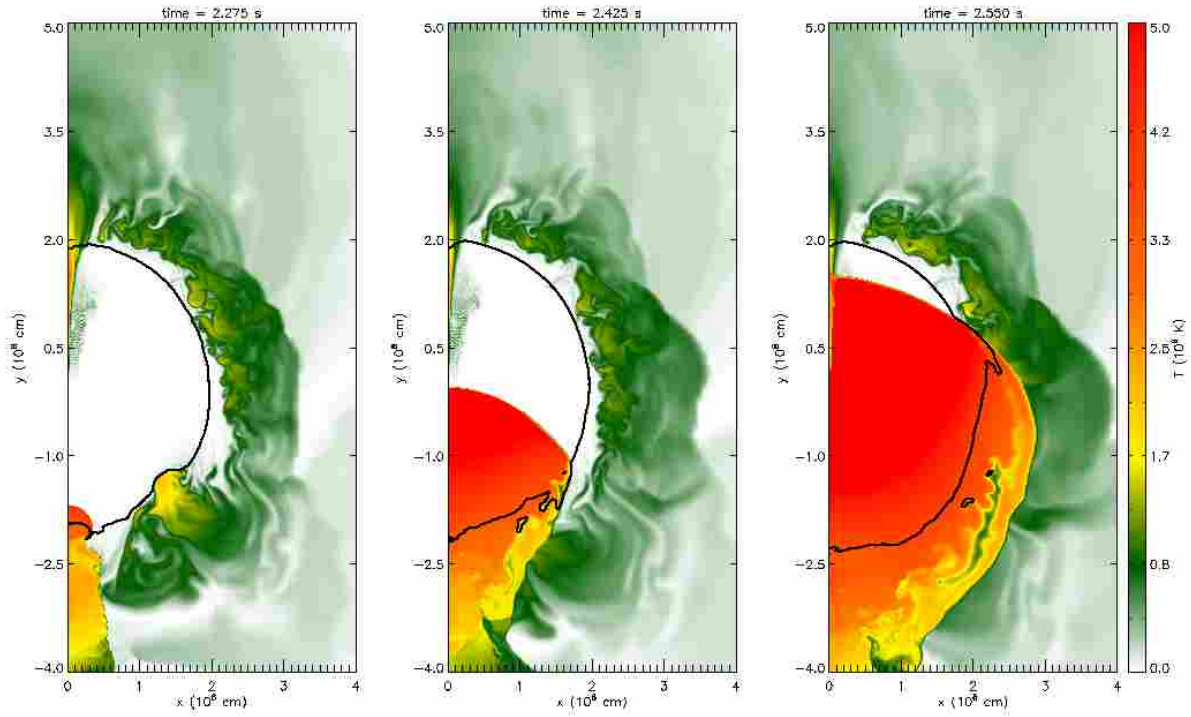


Fig. 5.— In this time sequence, the detonation wave breaks away from the jet in which it formed and sweeps across the stellar core. The black line is the  $10^7$  g/cm<sup>3</sup> iso-density contour which is roughly coincident with the stellar surface.

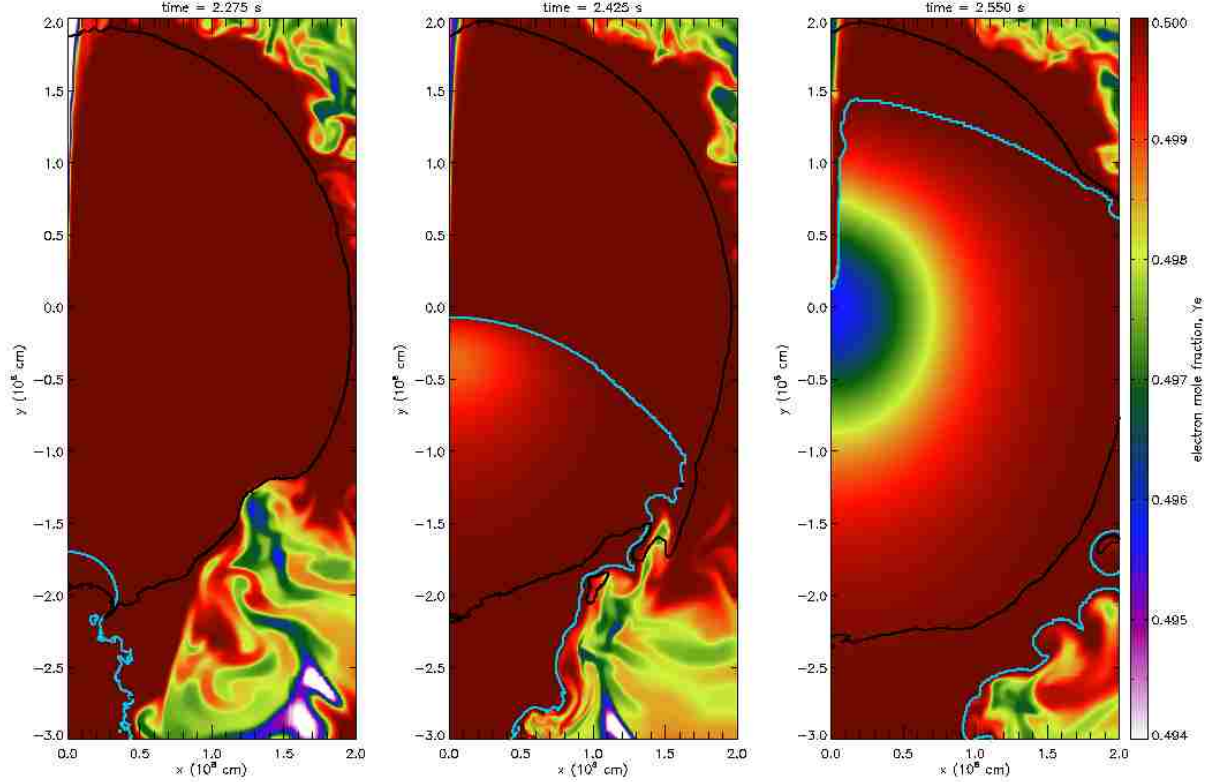


Fig. 6.— The time evolution of the electron mole fraction ( $Y_e$ ) is shown as the detonation wave passes over the stellar center. The dip in  $Y_e$  reveals that neutronization is taking place in the high density core where material has burned to NSE. The expansion which follows the detonation freezes the  $Y_e$  distribution as the material evolves into a supernova remnant. The neutron rich material (low  $Y_e$ ) which surrounds the stellar core is the ash from the deflagration which had burned at high densities before it erupted from the star and spread out over the surface. The black line is the  $10^7$  g/cm<sup>3</sup> iso-density contour and the light blue line indicates the contour of carbon depletion at the 99% level.

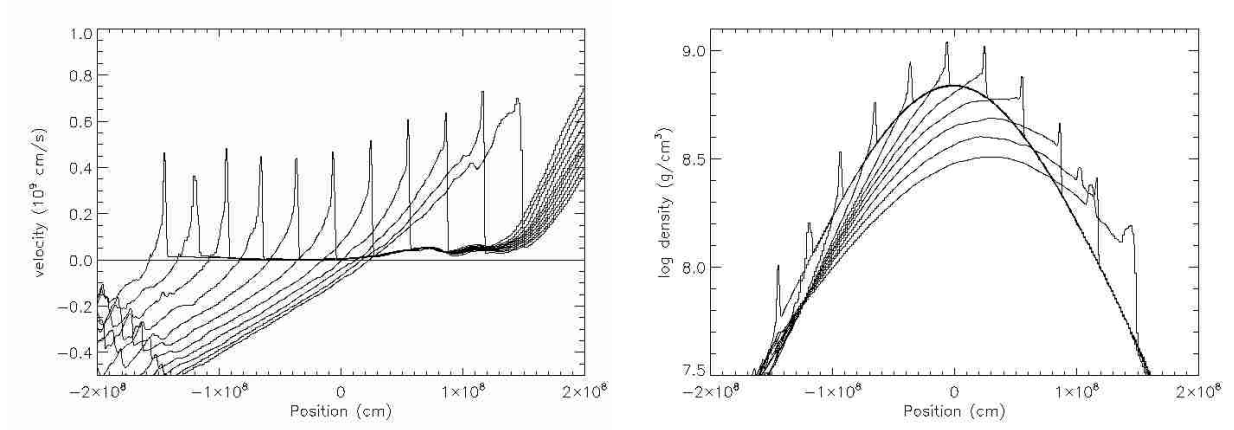


Fig. 7.— The profile of the (left) velocity and (right) density along the polar axis is shown for several moments evenly spaced in time ( $\delta t = 0.025 \text{ s}$ ) as the detonation wave passes across the stellar core for the model ignited with a flame bubble 40 km from the stellar center.

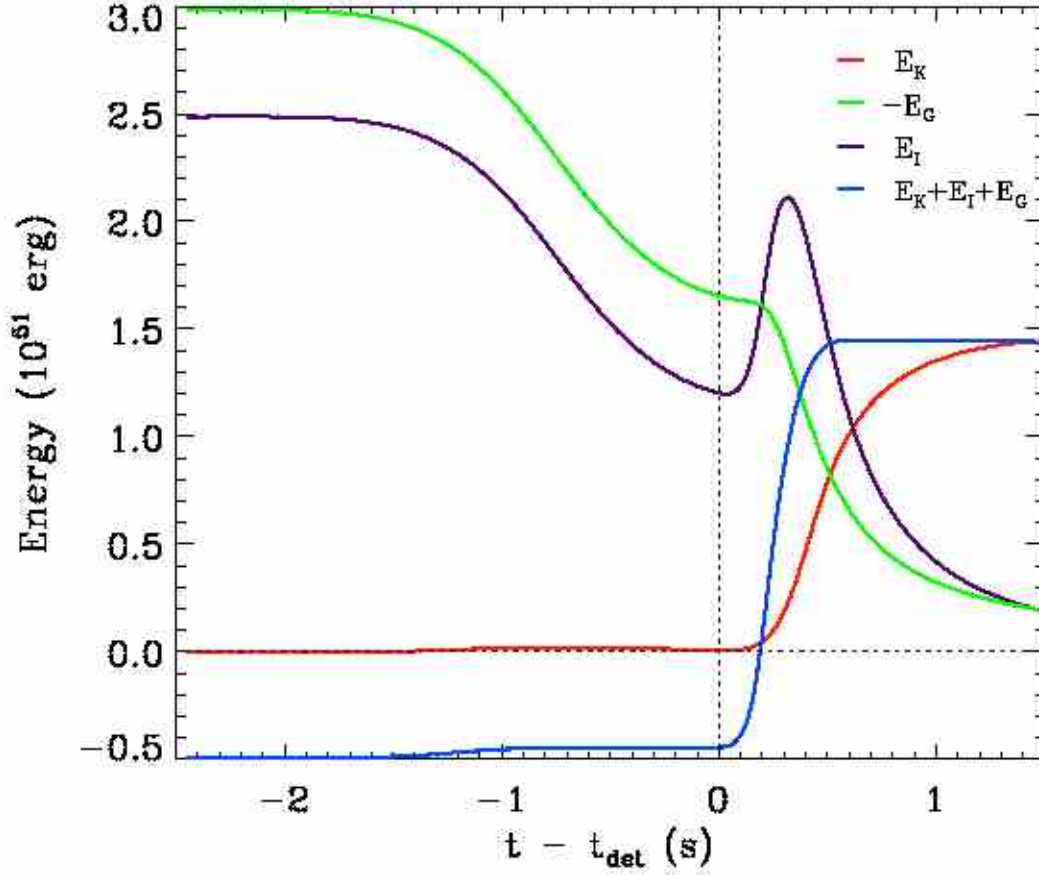


Fig. 8.— The time evolution of the kinetic, internal, and gravitational potential energy for a model with a flame bubble ignited 25 km from the stellar center. The nuclear energy released by burning in the deflagration ( $t < t_{det}$ , with  $t_{det} = 2.45$ s) and the detonation ( $t > t_{det}$ ) can be seen as a change in the sum of these three energy components (blue).

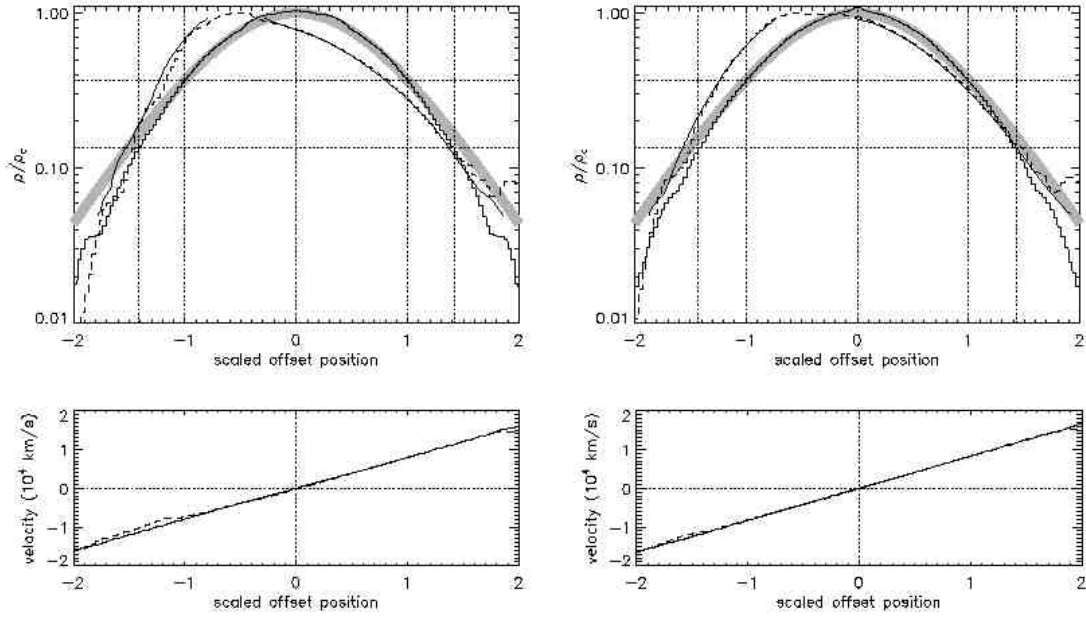


Fig. 9.— Late time ( $t > 4$  s) density and velocity profiles for post detonation state models having ignition: (left) 25 km and (right) 100 km off-center. The density is scaled by the peak value and the position is scaled by the density e-folding distance in the equatorial direction. The thick gray line shows the scaled density profile of the initial white dwarf model, while the post detonation state model is shown by thick black lines for profiles along the: (solid) equatorial, and (dashed) polar axes. The thin black line shows the reconstructed density profile along the polar axis based on the contour fits presented in Figure 11 (see text for more details).

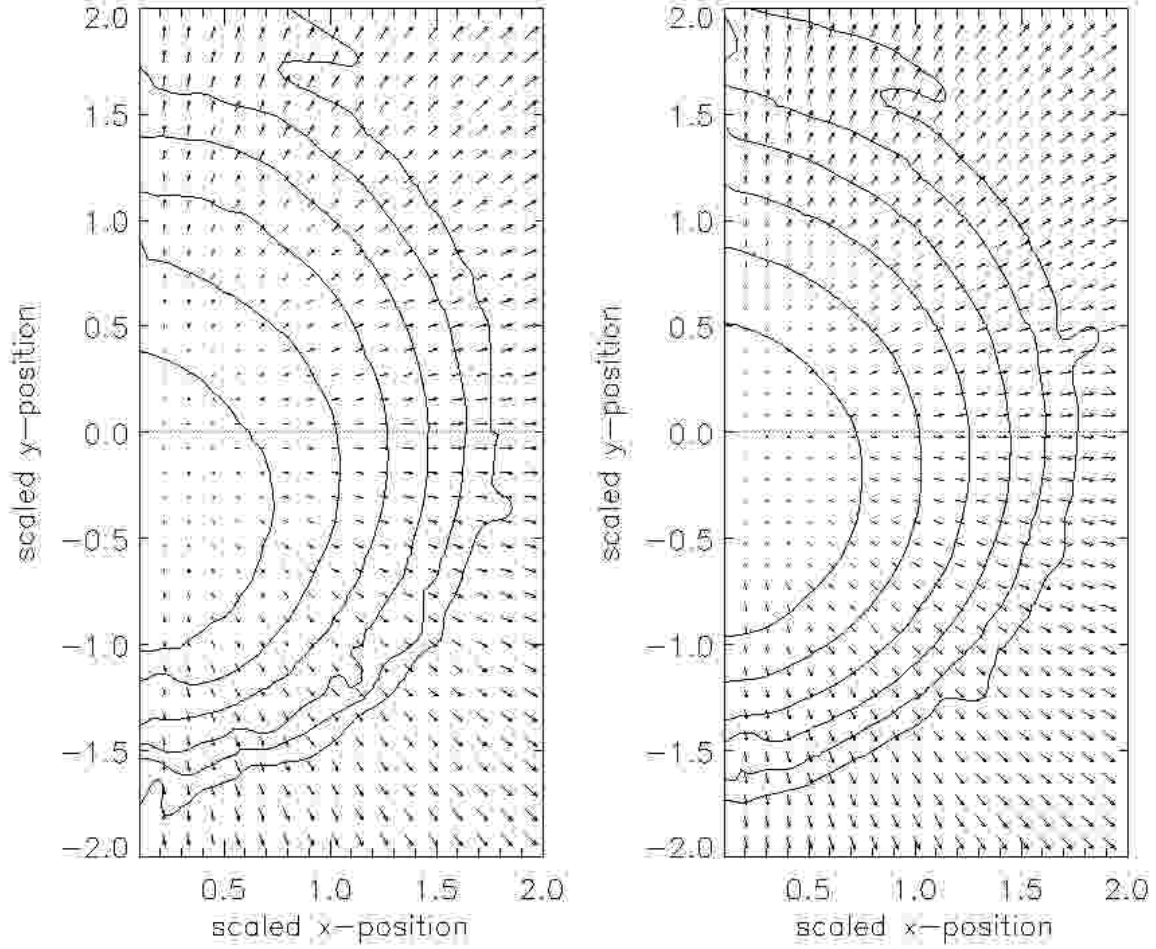


Fig. 10.— Late time ( $t > 4$  s) density contours for the models ignited: (left) 25 km, and (right) 100 km off-center. The contours mark the locations at which  $\ln(\rho/\rho_c) = -0.5, -1, -1.5, -2, -2.5$  where  $\rho_c$  is the peak density. The magnitude of the largest velocity vectors are (left)  $v = 2.4 \times 10^9$  cm/s, and (right)  $v = 2.5 \times 10^9$  cm/s. The spatial scales are the same density e-folding lengths as in Figure 9.

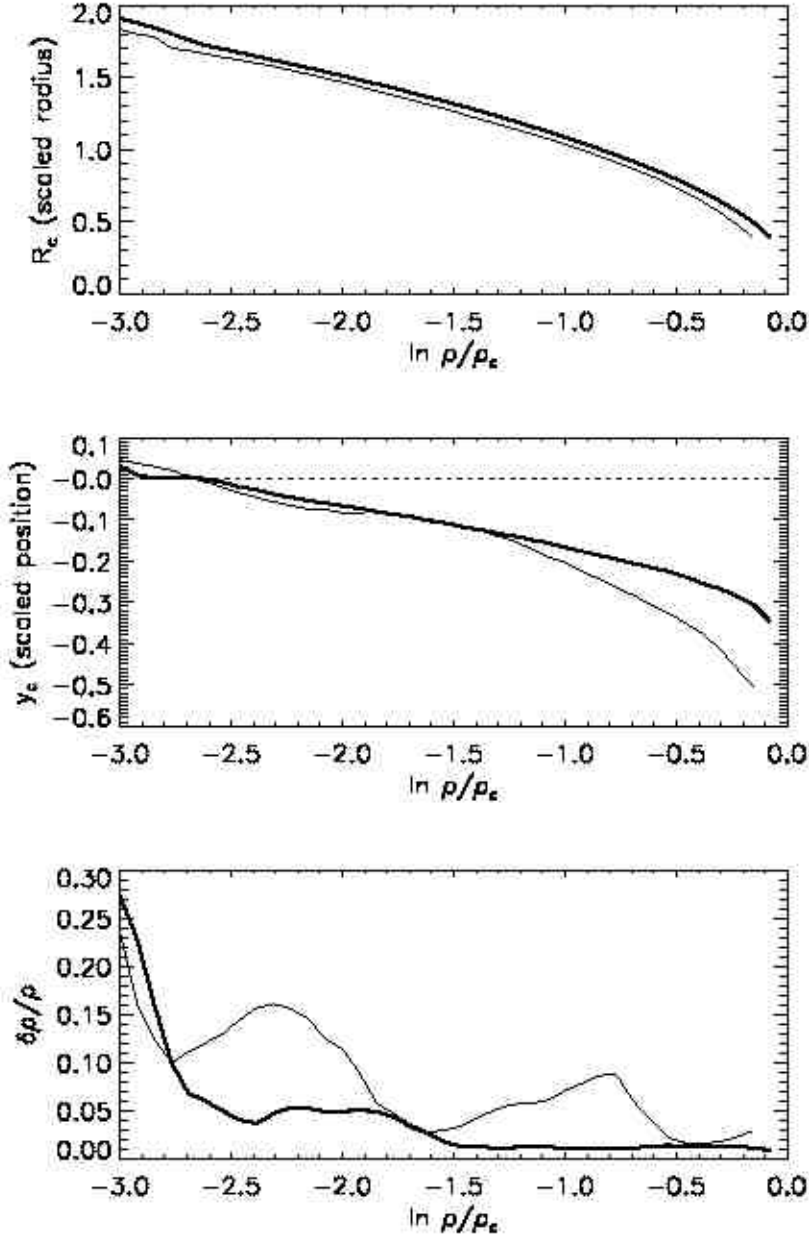


Fig. 11.— The iso-density contours of the remnant during late times ( $t > 4$  s, Figure 10) are well described by circles of radius  $R_c$  which have centers that are offset from the origin by an amount  $y_c$  along the symmetry axis. The best fit radii and offsets are shown here as a function of density contour value scaled to the central density for the models ignited 25 km (thin-line), and 100 km (thick-line) off-center in the panels above: (top) radius,  $R_c$ ; (middle) circle center,  $y_c$ . The spatial dimensions are scaled in terms of the e-folding density scale height in the equatorial direction of the remnant. (bottom) The degree of clumpiness is characterized by the ratio of the r.m.s. deviation in density along the best fit circle to the density contour value, denoted  $\delta\rho/\rho$ . The density perturbations at high density ( $\ln \rho/\rho_e > 1.5$ ) are due primarily to the narrow trail of ash left behind as the flame bubble rises out of the stellar core.

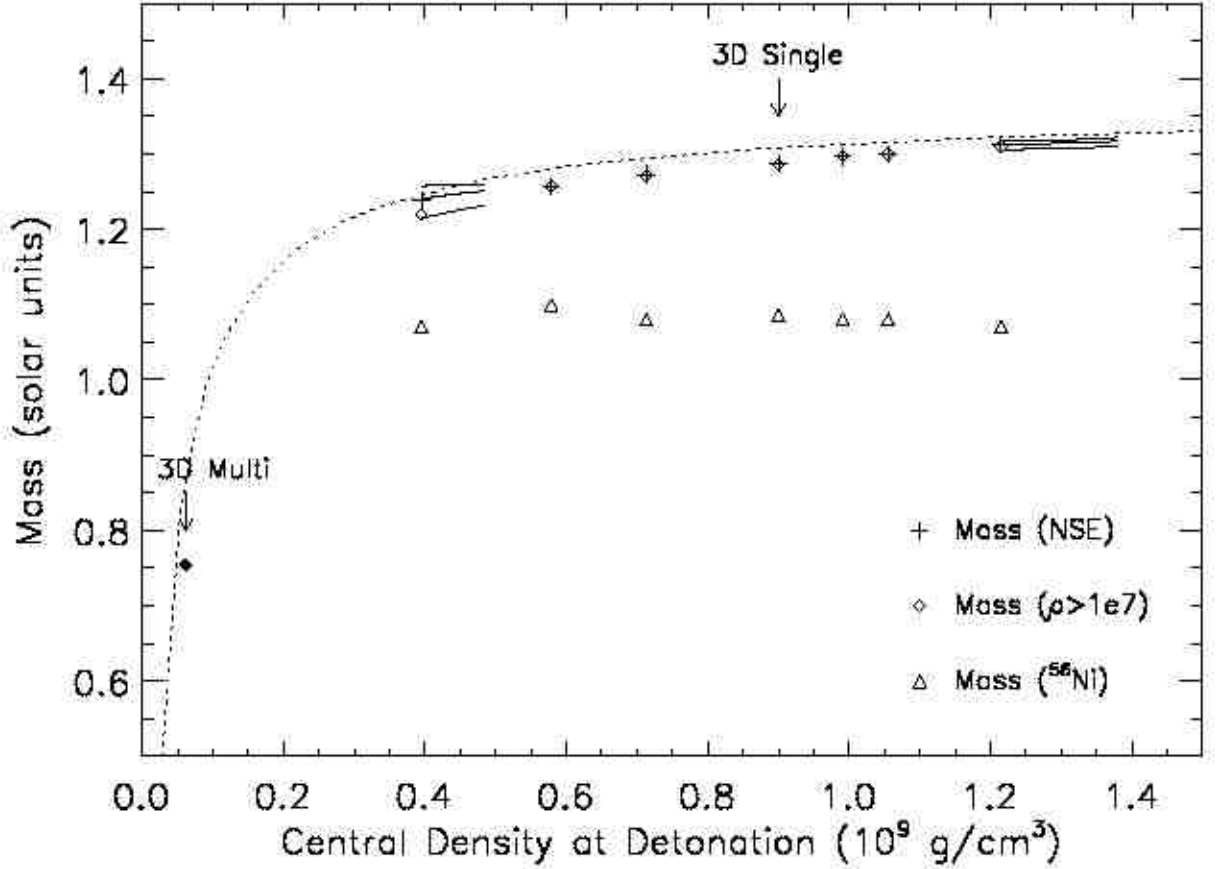


Fig. 12.— The total mass of NSE material and  $^{56}\text{Ni}$  created in the detonation and the total mass of high density ( $\rho > 10^7 \text{ g/cm}^3$ ) matter at detonation is plotted against the central density at detonation for all of the 2D models studied. The total mass of material having a density which exceeds  $\rho = 5 \times 10^6$ ,  $7.5 \times 10^6$ , and  $10^7 \text{ g/cm}^3$  during a 0.25 s time period preceeding detonation is shown by the curves which terminate at the detonation density for the 25 km and 100 km off-center ignition models. Data points for two 3D models are shown for comparison: the data points labeled “3D Single” show the  $^{56}\text{Ni}$ , NSE, and high density material masses for a 3D model ignited 80 km off-center. The data point labeled “3D Multi” shows the central density and the high density material mass for a 3D multi-point ignition model which is described in the text (see §5). The dashed line shows the relationship between central density and high density material for the initial white dwarf model expanded by the (linear) fundamental pulsation mode.



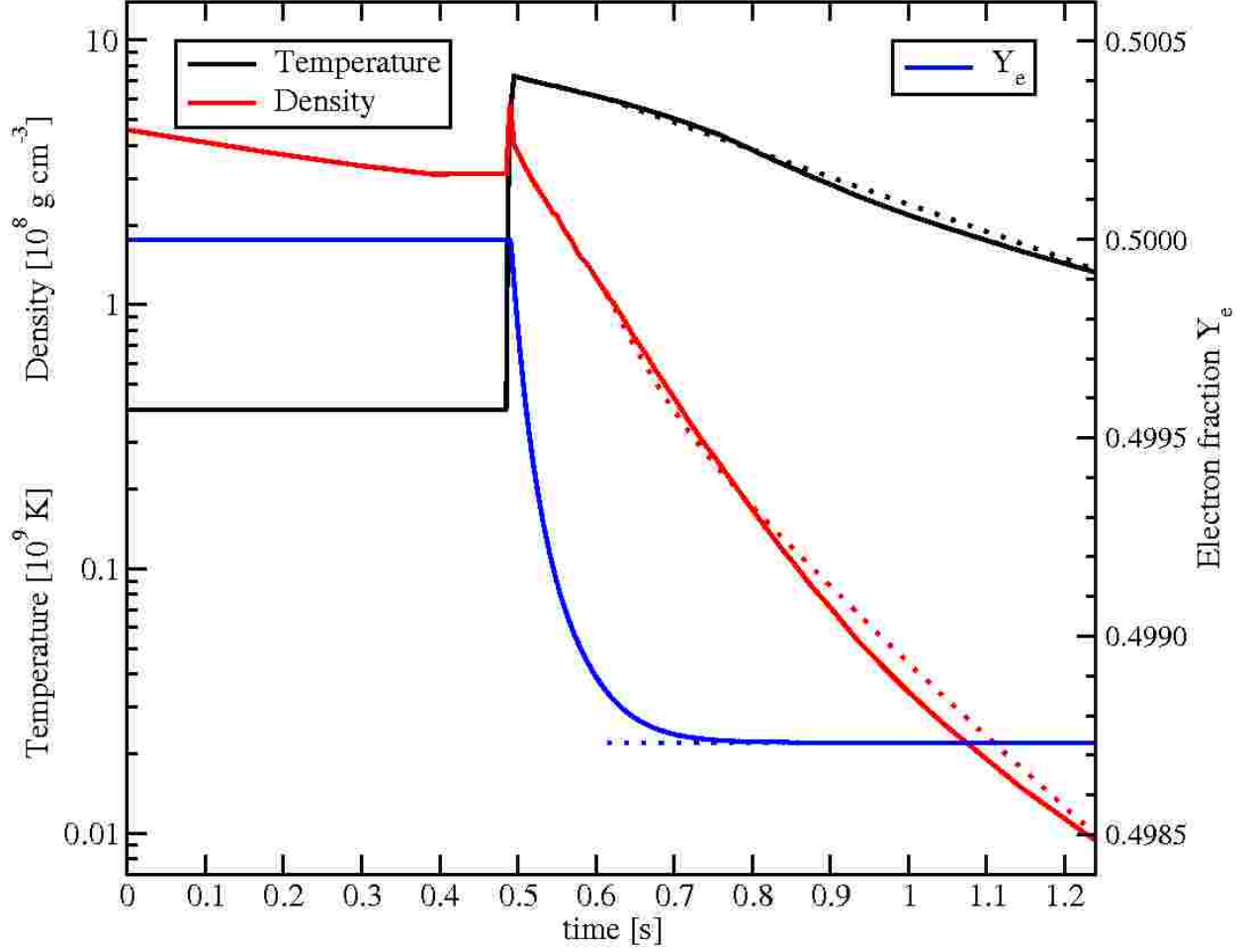


Fig. 13.— The thermodynamic trajectory of a Lagrangian tracer particle having an expansion timescale  $\tau = 0.42$ s, and final entropy  $s = 2.273 N_A k$  and final electron mole fraction  $Y_e = 0.49873$ . The dotted line shows the analytic adiabatic fit to this trajectory, parameterized by  $\tau$ ,  $Y_e$ , and  $s$ .

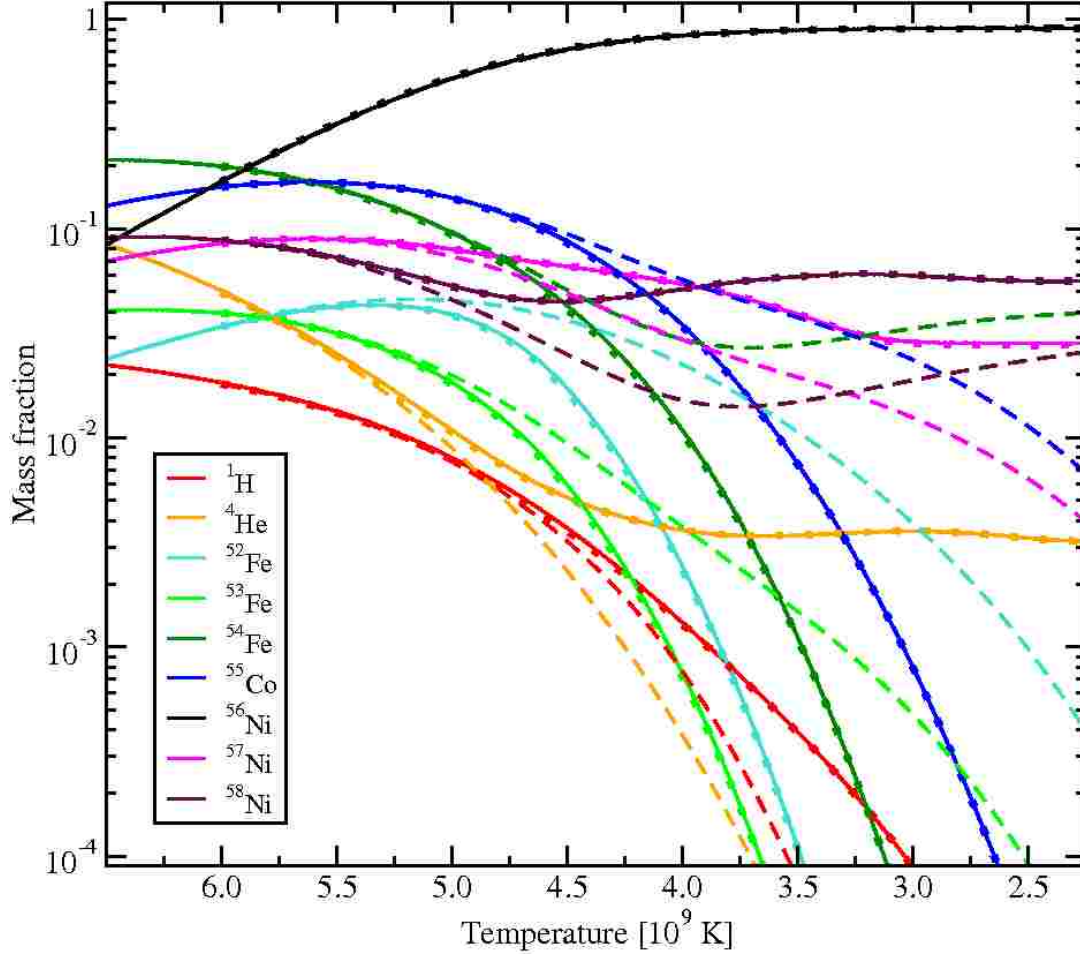


Fig. 14.— The time evolution is shown for various high abundance iron peak isotopes during the expansion which is here parameterized by the plasma temperature. For each species the abundances have been calculated with a network using the thermodynamic trajectory of the tracer particle (solid) and the analytic fit (dotted). For comparison, the NSE values are shown (dashed) using the thermodynamic conditions at each point along the particle trajectory. All three are in good agreement until  $T \sim 5.5 \times 10^9$  K, below which the NSE distribution begins to deviate from the network calculation at various temperatures. The tracer particle and the analytic fit agree to a high level of precision through freeze out.

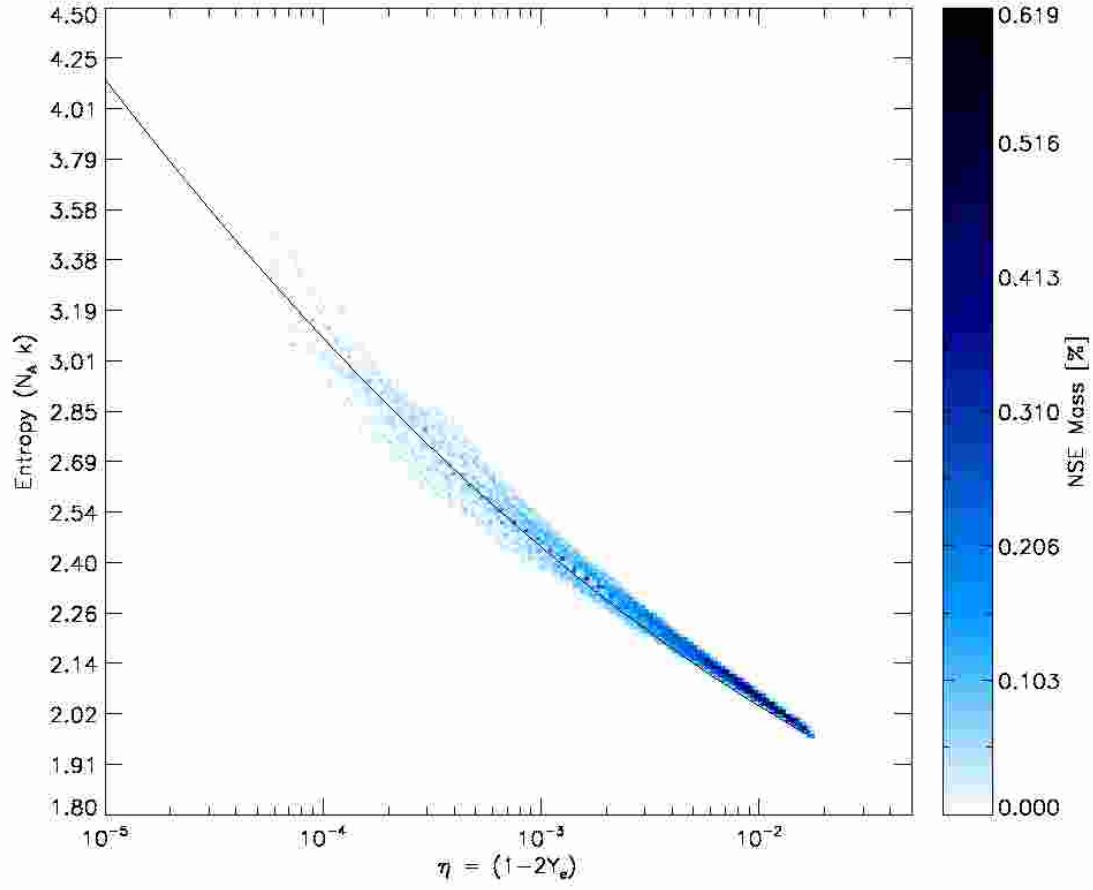


Fig. 15.— The distribution of NSE mass in entropy and degree of neutronization for the model with 100 km off-center bubble ignition. The black line indicates the curve on which the freeze out yield table was calculated (§5.1).

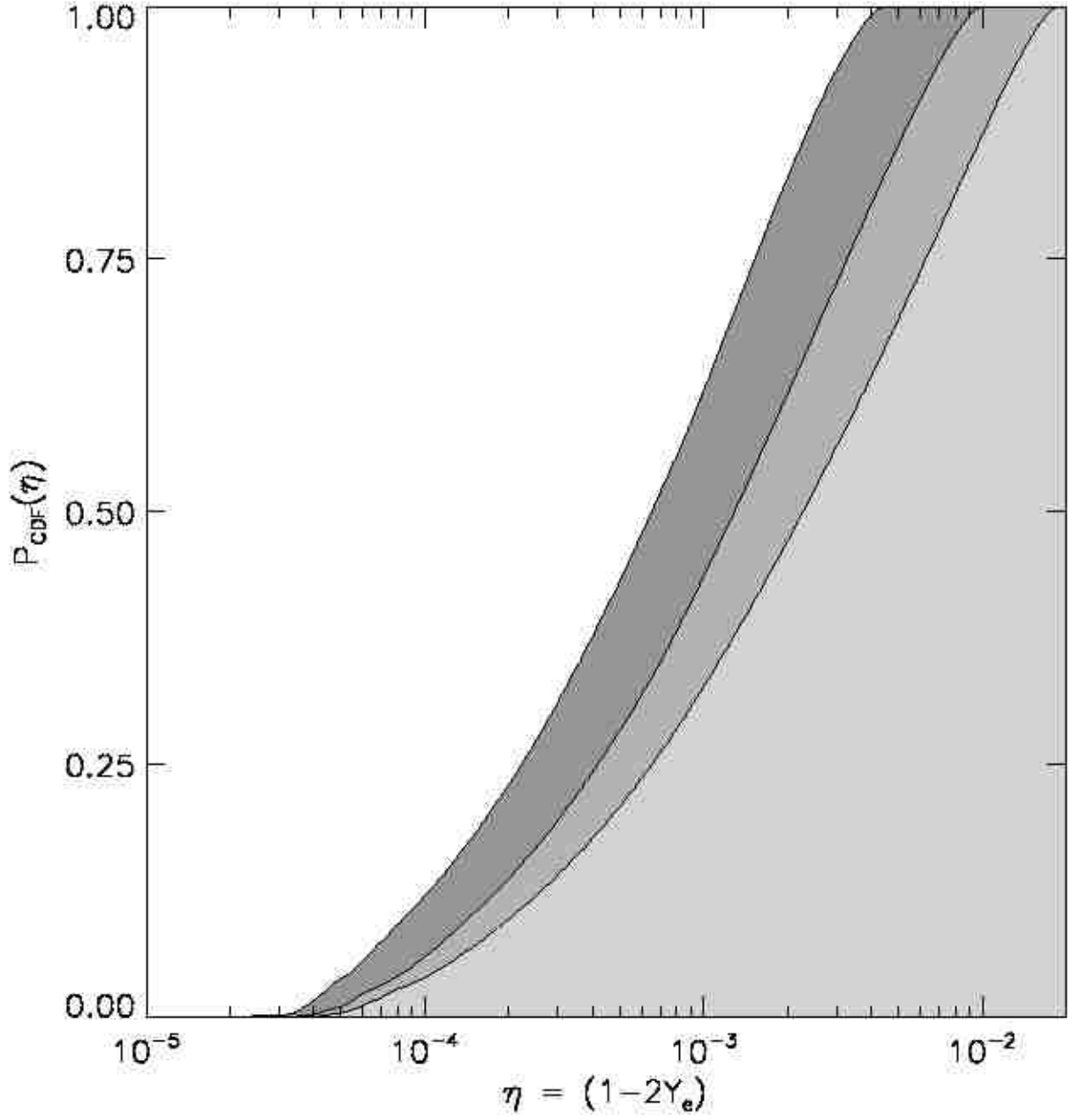


Fig. 16.— Cumulative distribution functions showing the fraction of NSE material below a certain degree of neutronization for the models ignited: 25 km, 40km, and 100 km off-center (from darkest to lightest, respectively).

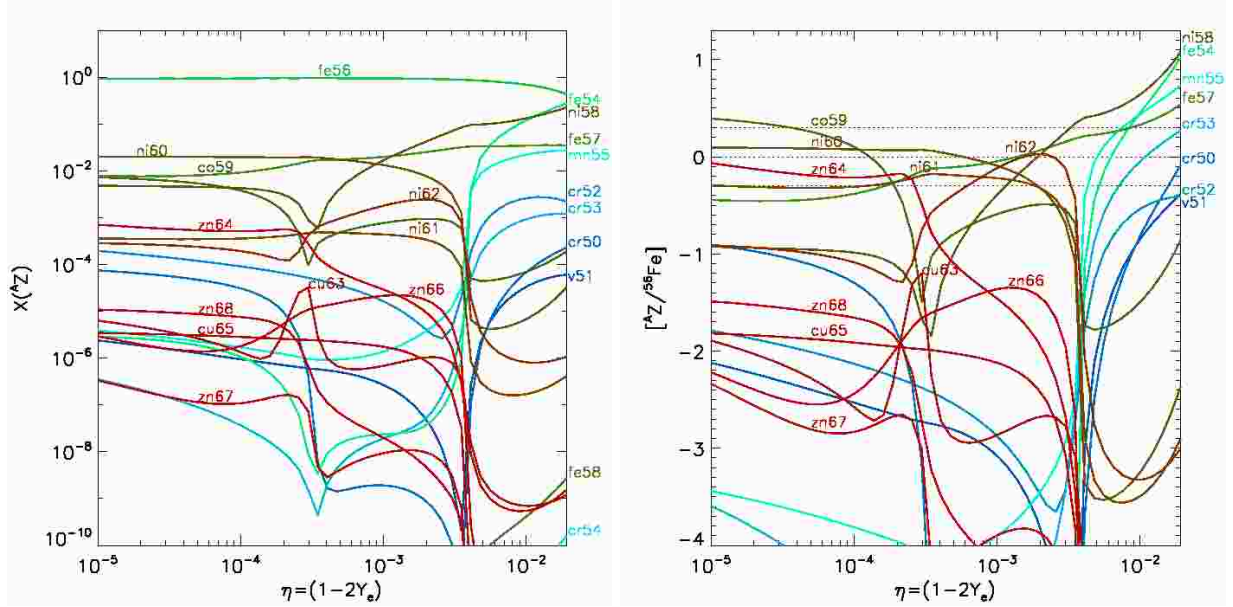


Fig. 17.— Iron peak freezeout yields, accounting for radioactive decay, as a function of the degree of neutronization. The corresponding entropy of the material is related to the degree of neutronization,  $S_f = S_f(\eta_f)$ , by the black line shown in Figure 15 and an expansion timescale of  $\tau = 0.4$  s. (left) Isotope mass fractions,  $X(^AZ)$  for nuclide with atomic number  $A$  and proton number  $Z$ . (right) Isotope mass fractions scaled to  $X(^{56}\text{Fe})$  and normalized to the corresponding solar system abundance ratios of Lodders (2003) where  $[^AZ/^{56}\text{Fe}] = \log_{10}(X(^AZ)/X(^{56}\text{Fe})) - \log_{10}(X(^AZ)/X(^{56}\text{Fe}))_{\odot}$ . The dashed horizontal lines indicate where the scaled abundance ratio is equal to 0.5, 1.0, and 2.0 times the solar system value.

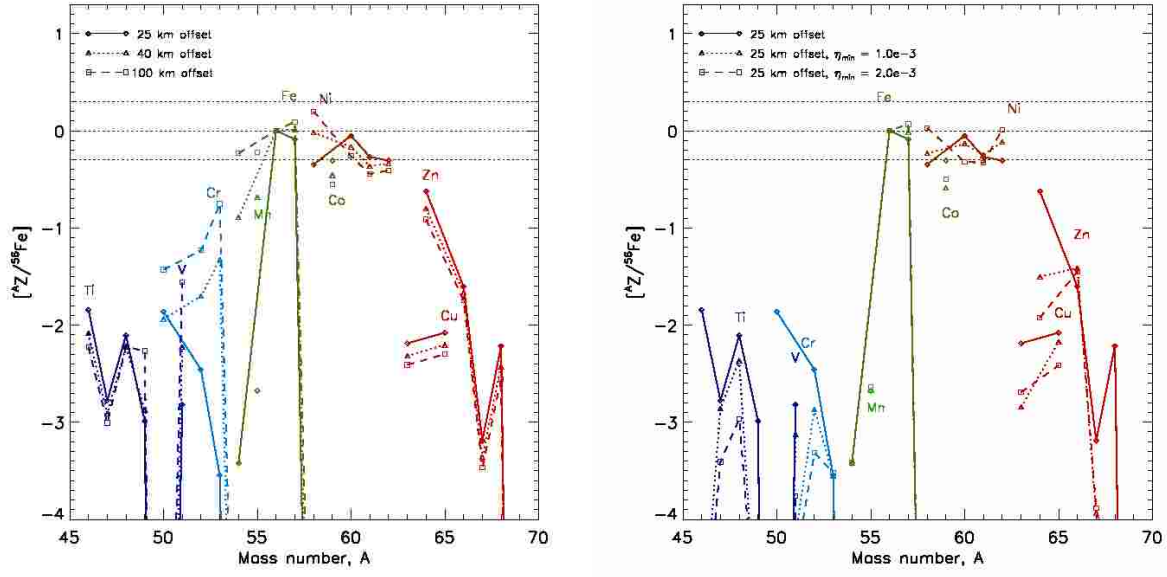


Fig. 18.— (left) The nucleosynthetic yields normalized by the solar system abundances are shown for three models which span the degree of pre-expansion and neutronization in our simulation suite. (right) The variation in the yields due to imposing a neutronization floor of  $\eta_{\min} = 0$ ,  $10^{-3}$ , and  $2 \times 10^{-3}$  for the model ignited 25 km off-center. Same notation as Figure 17

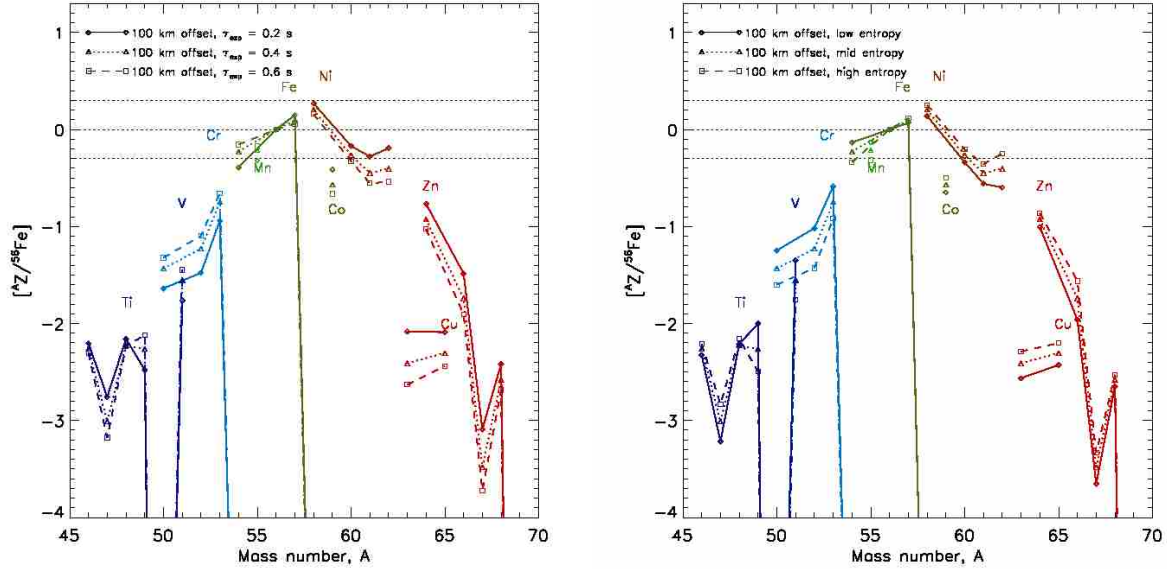


Fig. 19.— The variation in nucleosynthetic yields due to: (left) variations in expansion timescale, with  $\tau_{\text{exp}} = 0.2, 0.4$ , and  $0.6$  s; and (right) entropy changes, where  $\pm 5\%$  variations about the fiducial entropy-neutronization curve,  $S_f = S_f(\eta_f)$ , shown in Figure 15 have been used. Same notation as Figure 17.

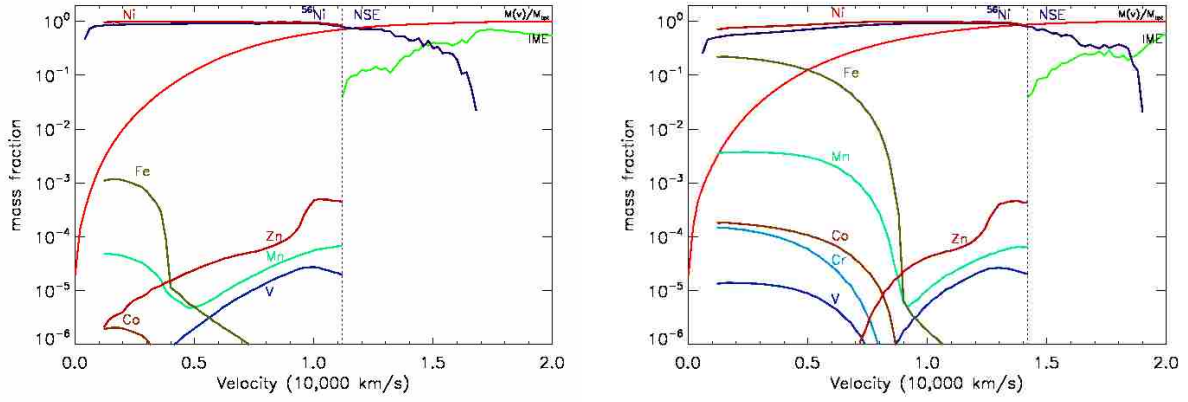


Fig. 20.— Distribution of elemental abundances are shown as a function of expansion velocity for models having initial flame bubbles ignited (left) 25 km and (right) 100 km from the stellar center. The elemental yields are calculated by taking into account radioactive decays with half lives less than 1 day. The dotted vertical line indicates the velocity above which less than 95% of the material has been burned to NSE and therefore our nucleosynthesis post-processing method (§5.1) is no longer reliable. At velocities where less than 95% of the material burns to NSE we show only the total fraction of NSE and intermediate mass elements (IMEs). The red curve shows the fraction of the total stellar mass interior to the velocity.

Table 1. Simulation Model Parameters

$r_{\text{off}}$ (km)	$t_{\text{det}}$ (s)	$r_{\text{det}}$ ( $10^3$ km)	$E_{\text{n,def}}$ ( $10^{49}$ erg)	$M_{\text{def}}$ ( $M_{\odot}$ )	$M_{\text{def}}^{\text{IME}}$ ( $M_{\odot}$ )	$M_{\text{def}}^{\text{NSE}}$ ( $M_{\odot}$ )	$M_{\text{det}}^{\text{IME}}$ ( $M_{\odot}$ )	$M_{\text{det}}^{\text{NSE}}$ ( $M_{\odot}$ )	$M[^{56}\text{Ni}]^{\text{a}}$ ( $M_{\odot}$ )	$E_{\text{tot}}^{\text{c}}$ $10^{51}$ erg
20	...	...	...	...	...	...	...	...	...	...
25	2.45	2.19	5.73	3.88(-2)	1.50(-2)	2.38(-2)	0.127	1.239	1.07	1.445
30	2.32	2.05 <sup>b</sup>	4.91	2.96(-2)	1.01(-2)	1.96(-2)	0.110	1.257	1.10	1.447
40	2.24	2.04	3.84	2.76(-2)	1.20(-2)	1.56(-2)	0.090	1.273	1.08	1.469
60	1.99	1.84	2.86	1.84(-2)	0.59(-2)	1.24(-2)	0.071	1.296	1.08	1.498
80	1.98	1.83	2.64	1.70(-2)	0.62(-2)	1.08(-2)	0.068	1.299	1.08	1.500
100	1.89	1.79	2.22	1.38(-2)	0.49(-2)	0.89(-2)	0.058	1.312	1.07	1.517

<sup>a</sup>The quoted  $^{56}\text{Ni}$  mass is that created in the detonation.

<sup>b</sup>off-axis detonation:  $(x, y) = (-2.04, 0.191) \times 10^8$  cm.

<sup>c</sup>The total energy at  $t=3.0$  s.

Table 2. 443 Nuclei Included in Network Calculations

Element	Z	A <sub>min</sub>	A <sub>max</sub>
n	0	1	1
H	1	1	1
He	2	3	4
C	6	12	12
O	8	16	22
F	9	16	24
Ne	10	16	26
Na	11	18	30
Mg	12	19	30
Al	13	22	33
Si	14	23	36
P	15	26	38
S	16	27	40
Cl	17	30	42
Ar	18	31	45
K	19	34	50
Ca	20	35	52
Sc	21	39	57
Ti	22	39	59
V	23	43	61
Cr	24	44	61
Mn	25	48	62
Fe	26	48	68
Co	27	51	66
Ni	28	52	70
Cu	29	55	72
Zn	30	56	74
Ga	31	60	74
Ge	32	62	76
As	33	67	78
Se	34	67	82
Br	35	71	81
Kr	36	71	86



Table 3. Scaled elemental Fe-peak yields,  $[X/Fe]$ , for select explosion models.<sup>a</sup>

${}^Z\text{X}$	$r_{\text{off}}=25$ km	$r_{\text{off}}=40$ km	$r_{\text{off}}=100$ km
${}^{46,47,48,49,50}\text{Ti}$	-2.12	-2.27	-2.29
${}^{50,51}\text{V}$	-2.79	-2.21	-1.57
${}^{50,52,53,54}\text{Cr}$	-2.43	-1.65	-1.18
${}^{55}\text{Mn}$	-2.65	-0.67	-0.23
${}^{59}\text{Co}$	-0.28	-0.44	-0.56
${}^{58,60,61,62,64}\text{Ni}$	-0.22	-0.06	0.08
${}^{63,65}\text{Cu}$	-2.12	-2.26	-2.38
${}^{64,66,67,68,70}\text{Zn}$	-0.89	-1.07	-1.20

<sup>a</sup>Here the total elemental abundance is the sum over the listed stable isotopes  ${}^Z\text{X}$  and is denoted  $X = \sum({}^Z\text{X})$ . The standard notation for the logarithmic abundance ratio relative to the solar system abundance ratio is used where  $[X/Fe] = \log_{10}(X/Fe) - \log_{10}(X/Fe)_{\odot}$ .

Table 4. Integrated Iron Peak Yields ( $M_{\odot}$ )

Nuclide	half life $\tau_{1/2}$	decay mode $\beta^-/\beta^+$	$r_{\text{off}}=25$ km		$r_{\text{off}}=40$ km		$r_{\text{off}}=100$ km	
			$M_i^0$	$M_i^f$	$M_i^0$	$M_i^f$	$M_i^0$	$M_i^f$
$^{43}\text{Ti}$	509 ms	$\beta^+$	9.78e-08	...	7.45e-08	...	5.93e-08	...
$^{44}\text{Ti}$	60.0 y	$\beta^+$	1.01e-05	...	7.22e-06	...	5.66e-06	...
$^{45}\text{Ti}$	184.8 m	$\beta^+$	3.09e-10	...	3.17e-10	...	6.84e-10	...
$^{46}\text{Ti}$	...	...	2.70e-11	3.27e-06	4.29e-10	1.89e-06	6.03e-09	1.36e-06
$^{47}\text{Ti}$	...	...	3.92e-15	3.50e-07	1.02e-14	2.60e-07	1.30e-13	2.07e-07
$^{48}\text{Ti}$	...	...	6.64e-16	1.67e-05	7.65e-16	1.29e-05	5.07e-15	1.28e-05
$^{49}\text{Ti}$	...	...	...	1.64e-07	...	2.16e-07	1.37e-20	8.66e-07
$^{46}\text{V}$	422.5 ms	$\beta^+$	4.34e-10	...	3.86e-10	...	3.23e-10	...
$^{47}\text{V}$	32.6 m	$\beta^+$	2.66e-08	...	2.29e-08	...	2.09e-08	...
$^{48}\text{V}$	15.97 d	$\beta^+$	6.12e-13	...	2.11e-12	...	1.80e-11	...
$^{49}\text{V}$	329 d	$\beta^+$	2.30e-14	...	2.72e-13	...	3.64e-12	...
$^{51}\text{V}$	...	...	3.85e-20	5.49e-07	1.91e-18	2.19e-06	4.61e-17	1.01e-05
$^{47}\text{Cr}$	500 ms	$\beta^+$	3.24e-07	...	2.37e-07	...	1.86e-07	...
$^{48}\text{Cr}$	21.56 h	$\beta^+$	1.67e-05	...	1.29e-05	...	1.28e-05	...
$^{49}\text{Cr}$	42.3 m	$\beta^+$	3.29e-10	...	1.23e-07	...	7.99e-07	...
$^{50}\text{Cr}$	...	...	6.85e-10	9.47e-06	2.61e-06	8.10e-06	2.19e-05	2.58e-05
$^{51}\text{Cr}$	27.7 d	$\beta^+$	7.25e-14	...	3.61e-10	...	3.82e-09	...
$^{52}\text{Cr}$	...	...	8.35e-15	4.83e-05	7.62e-11	2.80e-04	1.11e-09	8.19e-04
$^{53}\text{Cr}$	...	...	...	4.53e-07	3.29e-17	7.63e-05	7.14e-16	2.85e-04
$^{54}\text{Cr}$	...	...	...	2.06e-16	...	6.06e-13	1.29e-19	7.17e-12
$^{50}\text{Mn}$	283.88 ms	$\beta^+$	8.38e-10	...	9.03e-10	...	1.31e-09	...
$^{51}\text{Mn}$	46.2 m	$\beta^+$	1.38e-08	...	1.82e-06	...	9.84e-06	...
$^{52}\text{Mn}$	5.591 d	$\beta^+$	2.40e-11	...	2.63e-08	...	1.66e-07	...
$^{53}\text{Mn}$	3.74 My	$\beta^+$	1.12e-11	...	2.24e-08	...	1.87e-07	...
$^{54}\text{Mn}$	312.12 d	$\beta^+$	2.06e-16	...	6.06e-13	...	7.17e-12	...
$^{55}\text{Mn}$	...	...	7.21e-19	2.63e-05	2.41e-15	2.60e-03	3.72e-14	7.54e-03
$^{50}\text{Fe}$	155 ms	$\beta^+$	9.47e-06	...	5.48e-06	...	3.94e-06	...
$^{51}\text{Fe}$	305 ms	$\beta^+$	5.36e-07	...	3.71e-07	...	2.86e-07	...
$^{52}\text{Fe}$	8.275 h	$\beta^+$	4.83e-05	...	2.80e-04	...	8.19e-04	...
$^{53}\text{Fe}$	8.51 m	$\beta^+$	4.38e-07	...	7.63e-05	...	2.85e-04	...
$^{54}\text{Fe}$	...	...	2.45e-05	2.49e-05	8.50e-03	8.50e-03	3.85e-02	3.85e-02
$^{55}\text{Fe}$	2.737 y	$\beta^+$	5.79e-09	...	2.63e-06	...	1.56e-05	...
$^{56}\text{Fe}$	...	...	1.21e-10	1.07e+00	6.82e-08	1.08e+00	5.38e-07	1.07e+00
$^{57}\text{Fe}$	...	...	2.61e-17	2.05e-02	1.97e-14	2.62e-02	2.45e-13	3.11e-02
$^{58}\text{Fe}$	...	...	1.67e-20	2.48e-13	1.09e-17	2.57e-11	1.40e-16	1.60e-10
$^{54}\text{Co}$	192.23 ms	$\beta^+$	4.02e-08	...	9.85e-08	...	1.56e-07	...
$^{55}\text{Co}$	17.53 h	$\beta^+$	2.54e-05	...	2.59e-03	...	7.52e-03	...
$^{56}\text{Co}$	77.23 d	$\beta^+$	1.20e-07	...	1.13e-05	...	4.08e-05	...
$^{57}\text{Co}$	271.74 d	$\beta^+$	1.20e-08	...	1.42e-06	...	6.34e-06	...
$^{58}\text{Co}$	70.86 d	$\beta^+$	2.48e-13	...	2.57e-11	...	1.60e-10	...
$^{59}\text{Co}$	...	...	1.54e-15	1.67e-03	1.90e-13	1.20e-03	1.20e-12	9.55e-04
$^{55}\text{Ni}$	202 ms	$\beta^+$	9.36e-07	...	6.82e-07	...	5.38e-07	...
$^{56}\text{Ni}$	6.075 d	$\beta^+$	1.07e+00	...	1.08e+00	...	1.07e+00	...
$^{57}\text{Ni}$	35.6 h	$\beta^+$	2.05e-02	...	2.62e-02	...	3.11e-02	...
$^{58}\text{Ni}$	...	...	1.96e-02	2.10e-02	4.45e-02	4.54e-02	7.38e-02	7.44e-02
$^{59}\text{Ni}$	76 ky	$\beta^+$	5.26e-07	...	1.11e-05	...	2.91e-05	...
$^{60}\text{Ni}$	...	...	3.26e-08	1.66e-02	1.01e-06	1.28e-02	2.97e-06	1.03e-02
$^{61}\text{Ni}$	...	...	6.04e-14	4.42e-04	1.90e-12	3.62e-04	6.26e-12	2.95e-04
$^{62}\text{Ni}$	...	...	8.78e-17	1.31e-03	2.90e-15	1.23e-03	1.16e-14	1.05e-03
$^{58}\text{Cu}$	7.0 s	$\beta^+$	1.38e-03	...	8.78e-04	...	6.55e-04	...
$^{59}\text{Cu}$	0.46 s	$\beta^+$	5.30e-04	...	5.14e-04	...	4.40e-04	...
$^{60}\text{Cu}$	0.57 s	$\beta^+$	8.17e-07	...	9.25e-07	...	8.49e-07	...
$^{61}\text{Cu}$	0.27 s	$\beta^+$	6.44e-08	...	1.32e-07	...	1.66e-07	...

Table 4—Continued

Nuclide	half life $\tau_{1/2}$	decay mode $\beta^-/\beta^+$	$r_{\text{off}}=25$ km		$r_{\text{off}}=40$ km		$r_{\text{off}}=100$ km	
			$M_i^0$	$M_i^f$	$M_i^0$	$M_i^f$	$M_i^0$	$M_i^f$
$^{62}\text{Cu}$	0.19 s	$\beta^+$	7.53e-11	...	7.42e-11	...	6.89e-11	...
$^{63}\text{Cu}$	...	...	4.39e-14	3.69e-06	1.43e-13	2.77e-06	2.28e-13	2.23e-06
$^{65}\text{Cu}$	...	...	...	2.19e-06	...	1.66e-06	...	1.32e-06
$^{59}\text{Zn}$	182 ms	$\beta^+$	1.14e-03	...	6.73e-04	...	4.86e-04	...
$^{60}\text{Zn}$	2.38 m	$\beta^+$	1.66e-02	...	1.28e-02	...	1.03e-02	...
$^{61}\text{Zn}$	89.1 s	$\beta^+$	4.42e-04	...	3.62e-04	...	2.95e-04	...
$^{62}\text{Zn}$	9.186 h	$\beta^+$	1.25e-03	...	1.20e-03	...	1.02e-03	...
$^{63}\text{Zn}$	38.47 m	$\beta^+$	2.86e-07	...	2.97e-07	...	2.60e-07	...
$^{64}\text{Zn}$	...	...	3.28e-09	2.25e-04	4.33e-09	1.52e-04	4.10e-09	1.16e-04
$^{66}\text{Zn}$	...	...	6.17e-18	1.39e-05	5.82e-17	1.22e-05	7.54e-17	1.01e-05
$^{67}\text{Zn}$	...	...	...	5.41e-08	...	3.70e-08	...	2.85e-08
$^{68}\text{Zn}$	...	...	...	2.35e-06	...	1.46e-06	...	1.08e-06